Compression fronts from fast radio bursts

Andrei M. Beloborodov[1, 2]

[1] *Physics Department and Columbia Astrophysics Laboratory, Columbia University, 538 West 120th Street New York, NY 10027,USA*
[2] *Max Planck Institute for Astrophysics, Karl-Schwarzschild-Str. 1, D-85741, Garching, Germany*

ABSTRACT

When a fast radio burst (FRB) expands from its source through a surrounding tenuous plasma, it strongly heats and compresses the plasma at radii up to $\sim 10^{14}$ cm. The likely central engines of FRBs are magnetars, and their ambient plasma at radii $r \gg 10^{10}$ cm is a magnetized $e^{\pm}$ wind. We formulate equations describing the FRB-plasma interaction, solve them numerically, and provide an approximate analytical picture of the interaction. We find the following: (1) FRBs emitted at $r < r_{\rm stoch} \sim 10^{12}$ cm induce fast stochastic heating and strong compression of the wind, sweeping it like a broom. The outcome of this interaction is determined by the energy losses of the radio wave. We evaluate the parameter space where the FRB survives its interaction with the wind. (2) At radii $r > r_{\rm stoch}$, the FRB induces regular heating to the Lorentz factor $\sim a_0$, where $a_0 \propto r^{-1}$ is the wave strength parameter. At $r > r_{\star} \sim 10^{13}$ cm, the FRB drives a quasisteady compression wave in the wind, with compression factor $C_{\star} \approx 1 + a_0^2$. Both characteristic radii $r_{\rm stoch}$ and $r_{\star}$ scale with FRB luminosity L as $L^{1/3}$. FRBs avoid damping if they are released into the wind medium outside $r_{\rm damp} \sim 10^{11}$ cm.

Keywords: Magnetars (992); Plasma astrophysics (1261); Radio bursts (1339); X-ray transient sources (1852); Magnetohydrodynamics (1964); Radiative processes (2055)

1. INTRODUCTION

Observations of fast radio bursts (FRBs) demonstrate the existence of ultrastrong electromagnetic waves in the Universe. They have characteristic frequencies $\nu = \omega/2\pi \sim 1$ GHz and durations $T \sim 1$ ms (Petroff et al. 2019), and their dimensionless strength parameter is[1]

$$a \equiv \frac{e\langle E_{\rm wave}^2 \rangle^{1/2}}{mc\omega} \approx 16\, \nu_9^{-1} L_{42}^{1/2} r_{12}^{-1}, \qquad (1)$$

where $L = cr^2 \langle E_{\rm wave}^2 \rangle$ is the isotropic equivalent of wave luminosity; $\langle E_{\rm wave}^2 \rangle^{1/2}$ is the root-mean-square of the wave electric field when the wave expands to a radius r.

FRBs have to propagate through the ambient plasma surrounding the source. The likely central engines of FRBs are neutron stars, which are surrounded by electron-positron plasma. The plasma is strongly magnetized:

$$\sigma \equiv \frac{B^2}{4\pi\rho c^2} \gg 1, \qquad (2)$$

where the magnetic field B and density ρ are measured in the plasma rest frame. Near the neutron star, the

amb@phys.columbia.edu

[1] Throughout the paper we use notation Q_n for a quantity Q normalized to 10^n in CGS units, e.g. $\nu_9 = \nu/10^9$Hz.

plasma is locked in the closed magnetosphere, rotating with a period $P \sim 1 - 10$ s. Outside the light cylinder $R_{\rm LC} = cP/2\pi \approx 5 \times 10^9 (P/1\,{\rm s})$ cm, a relativistic wind flows from the magnetosphere, powered by the star's rotation. Both the magnetosphere and the wind have $\sigma \gg 1$ (see Cerutti & Beloborodov (2017) for a review).

The plasma around neutron stars is tenuous, however it can have a strong effect on FRB propagation. The radio wave with $a \gg 1$ accelerates plasma particles to high energies, and this process can damp the wave, in particular if the energized plasma experiences radiative losses. Strong radiative damping has been demonstrated for FRBs emitted near a magnetar and propagating through its equilibrium outer magnetosphere at radii $r \sim 10^8 - 10^9$ cm (Beloborodov 2021, 2024).

Recently, Sobacchi et al. (2024) suggested that FRBs are also damped by their interaction with the wind at $r \gg R_{\rm LC}$ and so may fail to escape even if they are emitted outside the magnetosphere. They argued that damping results from compression of the magnetized wind by the FRB, efficiently consuming FRB energy if it is emitted at $r \lesssim 10^{12}$ cm. Sobacchi et al. (2024) came to their conclusions by analyzing dynamical equations for particles in a GHz wave. They made, however, two assumptions: (1) that particles perform regular oscillations in the wave, neglecting the effect of resonant energy exchange found in Beloborodov (2022) (hereafter B22)

and (2) that the pattern of plasma dynamics is steady in the frame moving with the wave packet. As shown below, both assumptions are invalid at $r \lesssim 10^{12}$ cm.

The present paper revisits the FRB-wind interaction. The problem is formulated in section 2 and approached in two steps:

First, we use test-particle simulations to demonstrate two types of heating, regular and stochastic, of a plasma exposed to (and compressed by) an FRB (section 3). When the plasma magnetic field is increased by compression, regular oscillations of particles in the radio wave are changed to stochastic resonant heating. This change boosts the heating and makes it irreversible.

Then, we examine how heating by the FRB results in the bulk acceleration and compression of the plasma. Heating determines acceleration because energy $\Delta\mathcal{E}$ received from the radio wave always comes with momentum $\Delta\mathcal{E}/c$ (the wave loses momentum $\Delta\mathcal{E}/c$). Plasma is accelerated and compressed on timescales much longer than the Larmor period and the wave oscillation period.[2] Therefore, it behaves as a fluid governed by magnetohydrodynamics (MHD). In section 4, we formulate MHD equations for the plasma bulk motion inside a propagating radio wave packet. These equations determine plasma compression by FRBs.

Before considering FRBs expanding through a radial wind, we examine the compression front in a plane geometry with a uniform background. First, we show that the problem has a simple steady-state solution (section 5). Its compression factor $C_\star$ is directly related to the particle energy gained from the radio wave and becomes huge for waves with strength parameter $a \gg 1$. Remarkably, $C_\star$ is independent of the plasma magnetization σ. This fact casts some doubt on the relevance of the steady-state solution; in particular, it clearly becomes irrelevant in the vacuum limit ($\sigma \to \infty$) where the radio wave should have no compression effect on a background magnetic field. A complete picture is revealed only by the full time-dependent solution (section 6). It shows that the MHD flow pattern in the propagating wave packet is gradually attracted to the steady state, and this relaxation takes a long time $t_\star$ proportional to σ. For propagation times $t < t_\star$, the steady state with large $C_\star$ is not reached; we evaluate the actual compression factor $C \ll C_\star$ in this situation.

These results allow one to investigate the FRB interaction with a magnetar wind in a broad range of radii. We describe the wind in section 7, and then investigate the compression front induced by the FRB in the wind. We identify two zones, with regular and stochastic heat-

ing, and find the transition radius r_{stoch} between them. Compression fronts from FRBs emitted in each zone are described in sections 8 and 9. FRB damping by its interaction with the wind is investigated in section 10. Our conclusions are summarized in section 11.

2. PROBLEM FORMULATION

2.1. *The role of magnetic field*

For an unmagnetized plasma, particle acceleration in a strong electromagnetic wave is a textbook problem (Landau & Lifshitz 1975) well known in the context of laser experiments (Bulanov et al. 2015). It was also discussed in the context of early pulsar models (Gunn & Ostriker 1971). The wave accelerates initially static particles to Lorentz factors $\gamma = 1 + a^2/2$, and their average velocity is aligned with the wave propagation direction. This average motion gives the plasma the bulk Lorentz factor $\Gamma \approx a \gg 1$.

The problem qualitatively changes when the background plasma is magnetized (B22). Now, in addition to the oscillating electromagnetic field of the wave, there is a background magnetic field $\boldsymbol{B}_{\mathrm{bg}}$, which arrests the particle motion across $\boldsymbol{B}_{\mathrm{bg}}$ and changes the frame where the particles have zero average momentum (the "fluid frame"). In the media surrounding FRB sources, B_{bg} is well below the radio wave amplitude E_0 at all radii $r > R_{\mathrm{LC}}$ considered in this paper. At the same time, B_{bg} far exceeds a minimum value sufficient to "magnetize" the plasma: the particle Larmor period is much smaller than the duration of the wave packet $T \sim 1$ ms. Besides the wave strength parameter a, the problem of wave-plasma interaction has two more dimensionless parameters: the plasma magnetization σ and the ratio of gyrofrequency $\omega_B = eB_{\mathrm{bg}}/mc$ to the wave frequency ω.

The ratio ω_B/ω plays a particularly important role. B22 showed that waves with $\omega > \omega_B$ drive a regular particle motion in the fluid frame: fast oscillations with wave frequency ω and Lorentz factor $\gamma \approx a$, superposed with (subdominant) slow gyration in the background magnetic field. If $1 < \omega_B/\omega < a$, gyration is accompanied by a resonant wave-particle interaction each Larmor period, leading to quick stochastic particle acceleration to $\gamma \gg a$. Oscillations in the wave then become energetically subdominant compared to the Larmor rotation with the stochastically pumped γ. The stochastic heating gives a well-defined mean expectation for the particle energy, which has been found analytically and confirmed numerically.

In addition to heating the plasma, the radio wave also deposits momentum, pushing the plasma along the wave direction. The effective inertia of a plasma with $\sigma \gg 1$ is increased by its magnetic field, which reduces its bulk acceleration. The bulk acceleration leads to compression of the plasma and its magnetic field (Beloborodov 2021).

Dynamics of a plasma exposed to the radio wave is easiest to investigate in the plane geometry, assuming a uniform magnetized background ahead of the wave.

---

[2] In simplest cases, the effect may be thought of as a ponderomotive force exerted by the wave. In the presence of strong radiative losses it is more appropriate to view it as a scattering process (B22). In any case, it is described from first principles by solving for the particle motion in the wave and finding $\Delta\mathcal{E}/c$.

Details of the radio wave are not important, however one needs to choose a concrete shape of the wave packet when simulating the plasma dynamics numerically.

2.2. Wave packet

As an example, consider a nearly harmonic plane electromagnetic wave with amplitude E_0, frequency ω, and duration $T \gg 2\pi/\omega$. Its strength parameter (defined in Equation (1)) is

$$a = \frac{a_0}{\sqrt{2}}, \qquad a_0 = \frac{eE_0}{mc\omega}. \tag{3}$$

The wave speed is weakly affected by the presence of a tenuous plasma, so it propagates with speed of light c. It will be convenient to use the coordinate

$$\xi \equiv t - \frac{z}{c}, \tag{4}$$

where the z-axis is chosen along the wave propagation direction. The radio wave packet is static in the ξ-coordinate and occupies the region $0 < \xi < T$. The wave amplitude is zero at the leading edge of the packet $\xi = 0$, rises on a timescale $\xi_{\mathrm{rise}} < T$, and then drops back to zero at $\xi = T$. In numerical examples we will use packets with the envelope

$$a(\xi) = a_{\max} \sin^2(\pi\xi/T), \qquad 0 < \xi < T. \tag{5}$$

The cold unperturbed medium ahead of the packet (at $\xi < 0$) will be called "upstream." The upstream medium is described by a uniform mass density ρ_{u} and a uniform magnetic field $\boldsymbol{B}_{\mathrm{u}}$. We will focus on the problem with $\boldsymbol{B}_{\mathrm{u}}$ oriented perpendicular to the wave propagation direction (as expected in winds, which carry magnetic fields transverse to the radial direction).

Two possible polarizations of the radio wave can be considered: the X-mode ($\boldsymbol{E}_{\mathrm{wave}} \perp \boldsymbol{B}_{\mathrm{u}}$) and the O-mode ($\boldsymbol{E}_{\mathrm{wave}} \parallel \boldsymbol{B}_{\mathrm{u}}$). We will use below the results of B22 for test-particle motion in the X-mode waves; similar results within numerical coefficients $\mathcal{O}(1)$ were recently published for the O-mode (Huang et al. 2024). The X-mode has the oscillating magnetic field $\boldsymbol{B}_{\mathrm{wave}}$ parallel to the background field $\boldsymbol{B}_{\mathrm{u}}$.

2.3. Plasma drift through the wave packet

The plasma behaves as an MHD fluid on timescales longer than the Larmor period. The fluid motion in the plane geometry with $\boldsymbol{B}_{\mathrm{u}}$ perpendicular to the z-axis is fully described by the drift velocity parallel to the z-axis,

$$\boldsymbol{\beta}_{\mathrm{D}} = \frac{\boldsymbol{v}_{\mathrm{D}}}{c} = \frac{\overline{\boldsymbol{E}} \times \overline{\boldsymbol{B}}}{\overline{B}^2}. \tag{6}$$

Here $\overline{\boldsymbol{E}}$ and $\overline{\boldsymbol{B}}$ are the MHD fields; the bar signifies averaging over a timescale longer than the Larmor time (and longer than the wave oscillation period). The average fields can also be denoted as $\boldsymbol{E}_{\mathrm{bg}}$ and $\boldsymbol{B}_{\mathrm{bg}}$ because

they serve as the effective background fields in the problem of particle motion in the wave, as described below.

A natural choice for a reference frame in the wave-plasma interaction problem is such that the upstream plasma is at rest. When discussing wave propagation in a wind, we will also view the problem in the lab frame where the upstream moves with a large speed $\beta_{\mathrm{u}} > 0$ along the wave propagation direction. In addition, frames with opposite motion, where the upstream plasma has $\beta_{\mathrm{u}} < 0$, may be useful in numerical simulations. In all these frames, $\boldsymbol{v}_{\mathrm{D}}$ is parallel to the z-axis, both outside and inside the wave packet. The fluid four-velocity u_{D}^{μ} then has two non-zero components:

$$u_{\mathrm{D}}^t = \gamma_{\mathrm{D}} = (1 - \beta_{\mathrm{D}}^2)^{-1/2}, \qquad u_{\mathrm{D}}^z = \gamma_{\mathrm{D}}\beta_{\mathrm{D}}. \tag{7}$$

Dynamical equations for u_{D}^{μ} and final results will be formulated in a Lorentz-invariant way, so they will hold for any frame boosted along z or, equivalently, any β_{u}.

Plasma with any speed $v_{\mathrm{D}} = dz/dt$ changes its ξ-coordinate with rate

$$\frac{d\xi}{dt} = 1 - \beta_{\mathrm{D}} > 0. \tag{8}$$

Thus, the MHD fluid always moves toward increasing ξ through the wave packet. When viewed in the rest frame of the upstream medium, the initially static fluid enters the wave packet at $\xi = 0$ and develops speed $\beta_{\mathrm{D}} \neq 0$ at $\xi > 0$. We wish to find the fluid motion in the packet, $\beta_{\mathrm{D}}(\xi)$, and the fluid compression factor $C(\xi) = \rho(\xi)/\rho_{\mathrm{u}}$.

3. PLASMA HEATING BY THE WAVE

The response of a magnetized plasma to a propagating radio wave packet can be disentangled if we first view the problem in the local fluid rest frame $\tilde{\mathcal{K}}$. In this frame, the wave-fluid interaction is reduced to a local heating effect: the strong high-frequency wave energizes particles to a Lorentz factor $\tilde{\gamma} \gg 1$.[3] This effect was calculated in B22 by tracking the motion of test particles exposed to the radio wave. The heating depends on the wave strength parameter a. For smooth packets, such that a varies on a scale $\Delta\tilde{\xi} \gg a\tilde{\omega}_B$ (typically satisfied by FRBs), the results for $\tilde{\gamma}$ may be summarized as follows.

(1) Waves with frequency $\tilde{\omega}$ exceeding the gyrofrequency $\tilde{\omega}_B = e\tilde{B}_{\mathrm{bg}}/mc$ drive regular particle oscillations with

$$\tilde{\gamma} = \sqrt{1 + a^2} \approx a \gg 1 \qquad (\tilde{\omega}_B < \tilde{\omega}). \tag{9}$$

Thus, the local $\tilde{\gamma}$ in the packet simply tracks the local strength parameter of the wave a.

(2) In the other heating regime, $1 < \tilde{\omega}_B/\tilde{\omega} < a$, the resonant pumping mechanism is activated, and the wave

---

[3] Hereafter, we use tilde to indicate that the quantity is measured in the local fluid frame $\tilde{\mathcal{K}}$. Tilde will be omitted if this does not lead to confusion. In particular, we omit tilde for thermodynamic quantities (which are defined only in frame $\tilde{\mathcal{K}}$, e.g. enthalpy w) and for a, since it is invariant under Lorentz boosts along z.

drives stochastic particle acceleration. Then, the average $\tilde{\gamma}$ inside a fluid element quickly exceeds a and keeps growing as the fluid moves through the wave packet (until radiative losses limit the growth or fluid exits behind the packet). The mean expectation for the particle Lorentz factor $\tilde{\gamma}$ grows according to the equation (B22,Beloborodov 2024)

$$\frac{d\tilde{\gamma}}{d\tilde{t}} = \chi \frac{a_0^2 \tilde{\omega}_B^{1/3} \tilde{\omega}^{2/3}}{\tilde{\gamma}^{4/3}} \qquad (1 < \tilde{\omega}_B/\tilde{\omega} < a_0), \qquad (10)$$

where $a_0^2 = 2a^2$, $\chi \sim 1$ is a numerical coefficient, and all quantities are measured in the fluid rest frame $\tilde{\mathcal{K}}$.

Calculations in B22 were performed assuming that the background magnetic field $\boldsymbol{B}_{\rm bg}$ is static, i.e. there is no background electric field $\boldsymbol{E}_{\rm bg}$ and hence no average particle drift: $\boldsymbol{v}_{\rm D}/c = \boldsymbol{E}_{\rm bg} \times \boldsymbol{B}_{\rm bg}/B_{\rm bg}^2 = 0$. This corresponds to using the frame $\tilde{\mathcal{K}}$ where the magnetized fluid is at rest — the energized particles have no net momentum as they gyrate in a static magnetic field. Note that the wave fields $\boldsymbol{E}_{\rm wave}$ and $\boldsymbol{B}_{\rm wave}$ oscillate around zero and do not contribute to the MHD fields $\overline{\boldsymbol{E}}$ and $\overline{\boldsymbol{B}}$ (averaged over a timescale longer than the particle Larmor period and the wave period). So, the MHD fields serve as the background fields in the test-particle calculations:

$$\overline{\boldsymbol{E}} = \overline{\boldsymbol{E}_{\rm bg} + \boldsymbol{E}_{\rm wave}} = \boldsymbol{E}_{\rm bg}, \quad \overline{\boldsymbol{B}} = \overline{\boldsymbol{B}_{\rm bg} + \boldsymbol{B}_{\rm wave}} = \boldsymbol{B}_{\rm bg}. \qquad (11)$$

In general, $\overline{\boldsymbol{E}} \neq 0$ which corresponds to a moving MHD fluid $v_{\rm D} \neq 0$. If $v_{\rm D}$ varies (the plasma is accelerated in the wave packet), no global inertial frame exists where the fluid would be static, and one has to consider the heating effect of the wave in a moving MHD fluid. Then, the test particle motion should be examined with $E_{\rm bg} \neq 0$.

Remarkably, the results found in B22 at $E_{\rm bg} = 0$ also hold in the accelerating background, as long as the particle motion is measured in the local drift frame $\tilde{\mathcal{K}}$ where $\tilde{\boldsymbol{E}}_{\rm bg} = 0$. This fact is illustrated below by direct calculations of particle motion in a wave packet with a non-static background field. We will prescribe smoothly varying fields $\boldsymbol{B}_{\rm bg}(\xi)$ and $\boldsymbol{E}_{\rm bg}(\xi)$ (varying on a scale much greater than the particle Larmor radius) and repeat the calculation of B22 for test particles.

In the simulations, we will use the frame where the upstream plasma is at rest, $\beta_{\rm D} = \beta_{\rm u} = 0$, and prescribe the background field of the form

$$B_{\rm bg} = \frac{\kappa^2 + 1}{2} B_{\rm bg}^{\rm u}, \qquad E_{\rm bg} = \frac{\kappa^2 - 1}{2} B_{\rm bg}^{\rm u}, \qquad (12)$$

$$\kappa \equiv \gamma_{\rm D}(1 + \beta_{\rm D}) = \frac{1}{\gamma_{\rm D}(1 - \beta_{\rm D})}. \qquad (13)$$

The upstream has $\kappa = \kappa_{\rm u} = 1$, $E_{\rm bg} = 0$, and $B_{\rm bg} = B_{\rm bg}^{\rm u}$. Fluid motion inside the wave packet is specified by a chosen function $\kappa(\xi)$. For the present purposes, Equation (12) may be viewed as an arbitrary prescription to test heating of fluid with a non-uniform motion $\beta_{\rm D}(\xi)$. As explained in next sections, any steady pattern of fluid motion in the wave packet satisfies Equation (12). It also satisfies $\tilde{\rho}/\kappa = const$ (uniform across the packet), where $\tilde{\rho} = \rho/\gamma_{\rm D}$ is the fluid proper density. Thus, the adopted prescription corresponds to a steady flow pattern with the proper compression factor $\tilde{\rho}/\tilde{\rho}_{\rm u} = \kappa/\kappa_{\rm u} = \kappa$. The magnetic field $\tilde{B}_{\rm bg}$ is frozen in the fluid and compressed by the same factor κ while $B_{\rm bg} = \gamma_{\rm D}\tilde{B}_{\rm bg}$ obeys Equation (12).

Our simulation will track a test particle initially located in the static upstream region and exposed to the propagating wave packet. The particle motion in the wave packet is found by solving the dynamical equation,

$$mc \frac{d\boldsymbol{u}}{dt} = e\left(\boldsymbol{E} + \boldsymbol{\beta} \times \boldsymbol{B}\right), \qquad (14)$$

where vector $\boldsymbol{u} = \gamma\boldsymbol{\beta}$ is the spatial part of the particle four-velocity; radiative losses are neglected here. The fields $\boldsymbol{E}(\xi)$ and $\boldsymbol{B}(\xi)$ include the background and wave fields: $\boldsymbol{E} = \boldsymbol{E}_{\rm bg} + \boldsymbol{E}_{\rm wave}$ and $\boldsymbol{B} = \boldsymbol{B}_{\rm bg} + \boldsymbol{B}_{\rm wave}$.[4]

3.1. Regular heating ($\tilde{\omega}_B < \tilde{\omega}$)

Let us prescribe $B_{\rm bg}(\xi)$ and $E_{\rm bg}(\xi)$ by choosing κ^2 of the form

$$\kappa^2 = 1 + \zeta a^2, \qquad (15)$$

where ζ is a constant coefficient. The prescribed $\kappa(\xi)$ implies the fastest drift of the fluid in the middle of the packet where $a(\xi)$ peaks (Equation 5); the fluid is static ahead and behind the wave packet where $a = 0$. The case of $\zeta = 0$ corresponds to a static magnetic background throughout the packet ($E_{\rm bg} = 0$); in this case, the particle motion is similar to that found in B22. When $\zeta \neq 0$, the presence of $E_{\rm bg} \neq 0$ changes the particle motion by introducing an additional electric force.

After solving for the oscillating particle motion in the wave packet, we calculate its Lorentz factor averaged over the wave oscillation period. Figure 1 shows the obtained Lorentz factor as a function of position ξ in the packet, in three sample models. The models have the same radio wave (packet with amplitude $a_{\rm max} = 4$) and different $\zeta = 0$, 0.4, and 1. The results demonstrate that the average particle Lorentz factor $\tilde{\gamma}(\xi)$ measured in the local fluid frame is the same in all three models, independent of the fluid motion in the packet, and follows the solution found with a static background (Equation 9). In the presented numerical models, we chose $\omega_B/\omega = 0.05$, where $\omega_B \equiv \tilde{\omega}_B^{\rm u}$ is the gyro-frequency in the upstream plasma. Then, the condition $\tilde{\omega}_B < \tilde{\omega}$ is satisfied throughout the packet, so the heating everywhere acts in the regular regime according to Equation (9).

---

[4] Notation here differs from B22 where $\boldsymbol{E}$ and $\boldsymbol{B}$ denoted the wave fields and the dynamical equation assumed $\boldsymbol{E}_{\rm bg} = 0$.
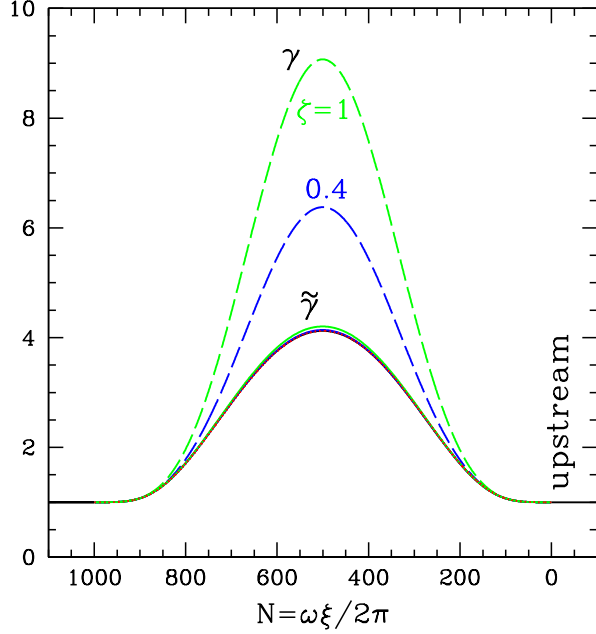
Figure 1. Lorentz factor γ of a test particle moving through the wave packet (averaged over the wave oscillation period). The upstream plasma is at rest ($\gamma = 1$) and has the gyrofrequency $\omega_B = 0.05\omega$. The plasma particle moves through the wave packet in the coordinate $\xi = t - z/c$ from right to left. The simulated packet consists of 10^3 oscillations with an envelope described by Equation (5) with $a_{\max} = 4$, and the background field is described by Equations (12) and (15). Different colors correspond to models with $\zeta = 0$ (static background, $E_{\mathrm{bg}} = 0$; black), $\zeta = 0.4$ (blue), and $\zeta = 1$ (green). For each model, dashed curve shows γ measured in the fixed frame (where the upstream plasma is at rest), and solid curve shows $\tilde{\gamma}$ measured in the local fluid rest frame. All solid curves overlap, demonstrating that $\tilde{\gamma}(\xi)$ is independent of the local fluid velocity $\beta_{\mathrm{D}} = E_{\mathrm{bg}}/B_{\mathrm{bg}}$ and follows the solution $\tilde{\gamma}^2 = 1 + a^2(\xi)$ (red dotted curve).

The test-particle motion changes if ω_B/ω is increased so that $\tilde{\omega}_B/\tilde{\omega}$ exceeds unity somewhere inside the packet, triggering stochastic acceleration. Compression of $\tilde{B}_{\mathrm{bg}}$ by the factor of κ implies $\tilde{\omega}_B = \kappa\omega_B$, and the Doppler-shifted wave frequency in the fluid frame is $\tilde{\omega} = \omega/\kappa$. This gives

$$\frac{\tilde{\omega}_B}{\tilde{\omega}} = \kappa^2 \frac{\omega_B}{\omega}. \tag{16}$$

In particular, in the model with $\kappa^2 = 1 + a^2$ and $a_{\max} = 4$, stochastic acceleration occurs if the upstream plasma has $\omega_B/\omega \gg (1 + a_{\max}^2)^{-1} = 1/17$. We have verified the transition to stochastic heating by running simulations with larger $\omega_B/\omega \gtrsim 0.1$.

3.2. Stochastic heating ($\tilde{\omega}_B > \tilde{\omega}$)

First, let us formulate the analytical prediction for stochastic heating by solving Equation (10) for $\tilde{\gamma}(\xi)$.

The fluid proper time $\tilde{t}$ is related to time t in the lab frame by $d\tilde{t} = dt/\gamma_{\mathrm{D}}$. During time dt, the fluid element moves in ξ by $d\xi = (1 - \beta_{\mathrm{D}})dt$, so

$$d\tilde{t} = \frac{d\xi}{\gamma_{\mathrm{D}}(1 - \beta_{\mathrm{D}})} = \kappa\, d\xi. \tag{17}$$

Using also $\tilde{\omega} = \omega/\kappa$ and $\tilde{\omega}_B = \kappa\omega_B$ (where $\omega_B \equiv \tilde{\omega}_B^{\mathrm{u}}$ is the upstream gyrofrequency), we rewrite Equation (10) as

$$\tilde{\gamma}^{4/3} \frac{d\tilde{\gamma}}{d\xi} = \chi a_0^2 \kappa^{2/3} \left(\omega_B\omega^2\right)^{1/3}. \tag{18}$$

For any chosen $\kappa(\xi)$, Equation (18) can be integrated for $\tilde{\gamma}(\xi)$, and this analytical prediction can be compared with simulations of test particle motion. Unlike regular heating (where $\tilde{\gamma}$ tracks the rise and drop of a), stochastic heating gives a monotonically growing mean expectation $\tilde{\gamma}(\xi)$: $d\tilde{\gamma}/d\xi \geq 0$.

Our simulation setup is described above; in particular, B_{bg} and E_{bg} are given by Equation (12). We arbitrarily choose $\kappa(\xi)$ of the form,[5]

$$\kappa = \begin{cases} 1 + (\kappa_0 - 1)\sin^2(\pi\xi/T) & \xi < T/2 \\ \kappa_0 & \xi > T/2 \end{cases} \tag{19}$$

so $\kappa(\xi)$ grows until it reaches κ_0 in the middle of the wave packet and stays constant in the second half of the packet. We have calculated particle motion in packets with $\kappa_0 = 1$ (no fluid motion, $\beta_{\mathrm{D}} = 0$) and $\kappa_0 = 3$.

The stochastic nature of heating requires calculations of many realizations of particle motion in the packet. We draw 4000 particles from an initial Maxwellian distribution with a small temperature $kT = 10^{-2}mc^2$, seeding small initial perturbations for the stochastic behavior. The particle motion is followed for each of the 4000 realizations, and the result is averaged to find the mean expectation for $\tilde{\gamma}(\xi)$.

The results are shown in Figure 2 for $\omega_B/\omega = 2$ and $a_0 = 30$. In both shown cases, $\kappa_0 = 1$ and $\kappa_0 = 3$, the found $\tilde{\gamma}(\xi)$ is in good agreement with the analytical prediction given by Equation (18) with $\chi \approx 2/3$.

In summary, the results of B22 for regular and stochastic heating hold in the local frame $\tilde{\mathcal{K}}$ regardless of fluid motion, as long as the fluid speed varies on timescales much longer than the Larmor period of particles. The Lorentz factor $\tilde{\gamma} \gg 1$ implies a strong heating effect, giving the fluid a relativistic effective temperature. The energized particles gyrate in the plane perpendicular to B_{bg}, so the plasma behaves as a two-dimensional relativistic gas. Its internal energy density U_{p} and pressure P_{p} (measured in frame $\tilde{\mathcal{K}}$) are

$$U_{\mathrm{p}} = 2P_{\mathrm{p}} = (\tilde{\gamma} - 1)\tilde{\rho}c^2, \qquad \tilde{\rho} = \frac{\rho}{\gamma_{\mathrm{D}}}. \tag{20}$$

---

[5] Plasma in packets with monotonically growing $\tilde{\gamma}(\xi)$ is expected to have a monotonically growing $\kappa(\xi)$. Therefore, in sample models of stochastic heating we choose $\kappa(\xi)$ that satisfy $d\kappa/d\xi \geq 0$.
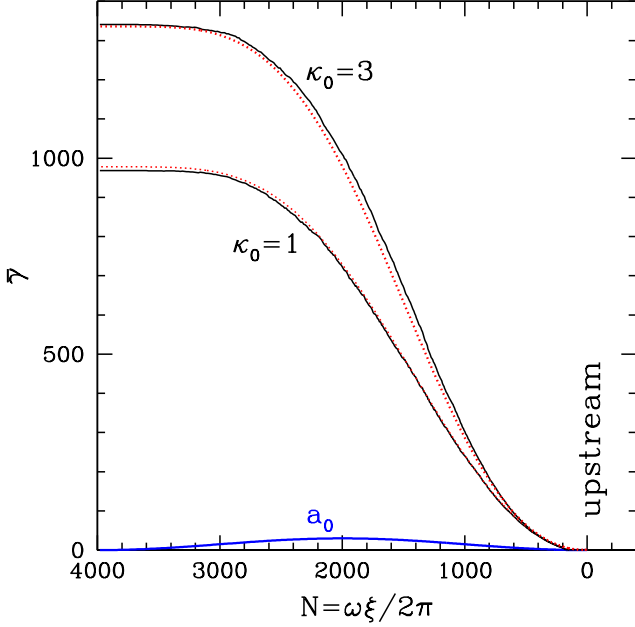
Figure 2. Average Lorentz factor $\tilde{\gamma}$ (measured in the local fluid rest frame) of particles crossing the wave packet in the regime of stochastic heating ($\tilde{\omega}_B > \tilde{\omega}$). The average $\tilde{\gamma}$ is calculated by tracking 4×10^3 test particles. The upstream plasma is at rest ($\gamma_D = 1$) and has a small temperature $kT = 10^{-2}mc^2$; its gyro-frequency is $\omega_B = 2\omega$. The packet $0 < \xi < T$ consists of $N = 4 \times 10^3$ oscillations; its envelope $a_0 = \sqrt{2}a$ is described by Equation (5) with $a_0^{\max} = 30$ (blue curve). Background field is described by Equations (12) and (19). As one can see in the figure, the plasma experiences heating as it moves through the wave ($\tilde{\gamma}$ grows with ξ). Black solid curves show the simulation results for $\kappa_0 = 1$ (static background field, no bulk motion of the plasma) and $\kappa_0 = 3$ ($\beta_D^{\max} = 0.8$). The results approximately agree with the analytical prediction (Equation (18), red dotted curves) with $\chi = 0.66$ for $\kappa_0 = 1$ and $\chi = 0.67$ for $\kappa_0 = 3$.

The heated particles gyrate with the Larmor frequency $\tilde{\omega}_L = \tilde{\omega}_B/\tilde{\gamma} \ll \tilde{\omega}_B$. It is below the wave frequency $\tilde{\omega}$ in both heating regimes, $\tilde{\omega}_B < \tilde{\omega}$ and $\tilde{\omega}_B > \tilde{\omega}$ (B22).

4. MHD EQUATIONS FOR FLUID MOTION

In the test-particle numerical experiments described above, we prescribed an arbitrary pattern of the fluid drift speed $\beta_D(\xi)$. Our goal now is to find the actual pattern of fluid motion in the radio wave packet. It can be quantified by the profiles of two quantities: κ (related to β_D) and $\tilde{C} = \tilde{\rho}/\tilde{\rho}_u$ (the proper compression factor). They are equal, $\tilde{C} = \kappa$, when a steady pattern of fluid motion is established in the propagating wave packet, i.e. when κ and $\tilde{\rho}$ are functions of ξ only (see below). The full problem, however, involves evolving profiles. Therefore, we will formulate general MHD equations for $\kappa(t, \xi)$ and $\tilde{\rho}(t, \xi)$, allowing time dependence. We first

state the equations in the usual variables t, z and later switch to the more convenient coordinates t, ξ.

4.1. Conservation laws

Fluid motion in the wave packet obeys conservation of mass, energy, and momentum. They are formulated using mass four-flux $\tilde{\rho}u_D^\nu$ and stress-energy tensor $T^{\mu\nu}$. Only the t and z components are relevant in the plane-parallel problem.

Mass conservation for an MHD flow (assuming negligible $e^\pm$ creation/annihilation) reads

$$\partial_\mu(\tilde{\rho}u_D^\mu) = \partial_t\rho + \partial_z(\rho v_D) = 0. \qquad (21)$$

Contributions to $T^{\mu\nu}$ are made by the plasma, the MHD electromagnetic field, and the radio wave:

$$T^{\mu\nu} = T_p^{\mu\nu} + T_f^{\mu\nu} + T_w^{\mu\nu}. \qquad (22)$$

The relevant components of $T^{\mu\nu}$ are T^{tt}, T^{tz}, and T^{zz}. In particular, the wave stress-energy tensor is

$$T_w^{zz} = T_w^{tz} = T_w^{tt} = U = \frac{\langle E_{\text{wave}}^2 \rangle}{4\pi} = \frac{m\,\omega^2 a^2}{4\pi r_e}, \qquad (23)$$

where $r_e = e^2/mc^2$ is the classical electron radius.

The plasma stress-energy tensor is

$$T_p^{\mu\nu} = (\tilde{\rho}c^2 + U_p + P_p)u_D^\mu u_D^\nu + \eta^{\mu\nu}P_p, \qquad (24)$$

where $\eta^{\mu\nu}$ is the Minkowski metric. The plasma pressure P_p and internal energy U_p (Equation 20) are controlled by the wave strength $a(\xi)$. In particular, $\tilde{\gamma} = \sqrt{1 + a^2}$ in the regular heating regime ($\tilde{\omega}_B < \tilde{\omega}$).

Relevant components of the stress-energy tensor of the MHD electromagnetic field are

$$T_f^{tt} = T_f^{zz} = \frac{B^2 + E^2}{8\pi}, \qquad T_f^{tz} = \frac{EB}{4\pi}, \qquad (25)$$

Hereafter, we drop the bar in $\overline{E}$ and $\overline{B}$ — in all remaining sections, $\boldsymbol{E}$ and $\boldsymbol{B}$ will have the meaning of MHD fields averaged over the Larmor timescale. $T_f^{\mu\nu}$ may be re-written in a form similar to ideal fluid:

$$T_f^{\mu\nu} = (U_f + P_f)u_D^\mu u_D^\nu + \eta^{\mu\nu}P_f \qquad (\mu, \nu = t, z), \quad (26)$$

where

$$U_f = P_f = \frac{\tilde{B}^2}{8\pi}, \qquad \tilde{B} = \frac{B}{\gamma_D}. \qquad (27)$$

Note that the MHD electric field vanishes in the fluid frame (there is no plasma drift in frame $\tilde{\mathcal{K}}$ by definition). The magnetic field in the fluid frame $\tilde{B}$ controls the energy density and effective pressure $P_f = U_f$. Magnetic flux freezing in each fluid element implies

$$\frac{\tilde{B}}{B_u} = \frac{\tilde{\rho}}{\rho_u}. \qquad (28)$$

The total MHD stress-energy tensor may be summarized as follows

$$T_{\mathrm{MHD}}^{\mu\nu} = T_{\mathrm{p}}^{\mu\nu} + T_{\mathrm{f}}^{\mu\nu} = h\tilde{\rho}c^2 u_{\mathrm{D}}^{\mu} u_{\mathrm{D}}^{\nu} + \eta^{\mu\nu} P, \qquad (29)$$

where

$$h = 1 + w + \sigma, \qquad P = \tilde{\rho}c^2\left(\frac{w}{3} + \frac{\sigma}{2}\right), \qquad (30)$$

$$w \equiv \frac{U_{\mathrm{p}} + P_{\mathrm{p}}}{\tilde{\rho}c^2} = \frac{3}{2}(\tilde{\gamma} - 1), \quad \sigma \equiv \frac{\tilde{B}^2}{4\pi\tilde{\rho}c^2} = \frac{\tilde{\rho}}{\tilde{\rho}_{\mathrm{u}}}\,\sigma_{\mathrm{u}}. \quad (31)$$

Note that the stress-energy tensor of the MHD fluid depends on the strength parameter a of the wave it interacts with. In particular, in the regular heating regime, Equation (9) implies that the dimensionless enthalpy w tracks the local strength of the wave $a(\xi)$:

$$w \approx \frac{3}{2}a \qquad (\text{when } \tilde{\omega}_B < \tilde{\omega} \text{ and } a \gg 1). \qquad (32)$$

Interaction of the wave with the MHD fluid obeys energy and momentum conservation,

$$\partial_\nu \left(T_{\mathrm{MHD}}^{\mu\nu} + T_{\mathrm{w}}^{\mu\nu}\right) = -\tilde{n}\dot{\mathcal{E}}_e u_{\mathrm{D}}^{\mu}. \qquad (33)$$

The term $\tilde{n}\dot{\mathcal{E}}_e u^\mu$ is the radiative loss rate (per unit volume) of the plasma particles, which oscillate and gyrate in the wave; $\tilde{n} = \tilde{\rho}/m$ is the particle number density and $\dot{\mathcal{E}}_e$ is the emitted power per particle, which is a Lorentz-invariant quantity.

The power $\dot{\mathcal{E}}_e$ can be calculated in the fluid frame $\tilde{\mathcal{K}}$. When $\tilde{\omega}_B < \tilde{\omega}$, it is given by

$$\dot{\gamma}_e \equiv \frac{\dot{\mathcal{E}}_e}{mc^2} \approx \frac{2}{3}\frac{r_e}{c}\tilde{\omega}^2 a^2 \tilde{\gamma}^2. \qquad (34)$$

A similar expression (with the numerical coefficient $4/3$ instead of $2/3$) holds in the regime of stochastic heating, $\tilde{\omega}_B > \tilde{\omega}$ (B22). The strength parameter of the radio wave a is invariant, and its frequency ω and electric field E_{wave} transform to the fluid frame as

$$\frac{\tilde{\omega}}{\omega} = \frac{\tilde{E}_{\mathrm{wave}}}{E_{\mathrm{wave}}} = \kappa^{-1}, \qquad (35)$$

where κ is defined in Equation (13). Equation (34) may also be written in terms of the wave energy density U,

$$\dot{\gamma}_e \approx \frac{\sigma_{\mathrm{T}}\tilde{U}}{mc}\tilde{\gamma}^2 = \frac{\sigma_{\mathrm{T}}U}{mc\,\kappa^2}\tilde{\gamma}^2, \qquad (36)$$

where $\sigma_{\mathrm{T}} = (8\pi/3)r_e^2$ is the Thomson cross section.

4.2. MHD equations in coordinates t, ξ

The conservation laws can also be stated using fluxes through the surfaces of $\xi = const$, which move with speed c. This will considerably simplify the analysis of wave-fluid interaction.

The fluid speed in the ξ-coordinate is $d\xi/dt = 1 - \beta_{\mathrm{D}}$, so the mass flux through a surface of $\xi = const$ is

$$F_{\mathrm{m}} = \rho(c - v_{\mathrm{D}}) = \frac{c\tilde{\rho}}{\kappa}. \qquad (37)$$

Mass conservation in the t, ξ-coordinates reads

$$\left.\frac{\partial\rho}{\partial t}\right|_\xi + \left.\frac{\partial F_{\mathrm{m}}}{\partial\xi}\right|_t = 0. \qquad (38)$$

Similarly, the flux of four-momentum $\mathcal{P}^\mu$ through a surface $\xi = const$ is $T^{\mu t} - T^{\mu z}$. Conservation of four-momentum (Equation 33) in the t, ξ-coordinates becomes[6]

$$\left.\frac{\partial T^{\mu t}}{\partial t}\right|_\xi + \frac{\partial}{\partial\xi}\left(T^{\mu t} - T^{\mu z}\right)_t = -\tilde{n}\dot{\mathcal{E}}_e u_{\mathrm{D}}^{\mu}. \qquad (39)$$

Note that the wave is static in ξ, so it creates no flux of energy or momentum across a surface of $\xi = const$:

$$T_{\mathrm{w}}^{\mu t} - T_{\mathrm{w}}^{\mu z} = U - U = 0 \qquad (\mu = t, z). \qquad (40)$$

Only the MHD fluid contributes to the fluxes. Thus, the fluxes of energy and momentum through a surface of $\xi = const$ are

$$\frac{F_{\mathrm{en}}}{c} = T_{\mathrm{MHD}}^{tt} - T_{\mathrm{MHD}}^{tz} = \frac{c^2\rho h}{\kappa} - P, \qquad (41)$$

$$F_{\mathrm{mom}} = T_{\mathrm{MHD}}^{zt} - T_{\mathrm{MHD}}^{zz} = \frac{c^2\rho h}{\kappa}\beta_{\mathrm{D}} - P. \qquad (42)$$

4.3. Conservation of $\mathcal{Q}_\pm$

Instead of energy $\mathcal{E}$ and momentum $\mathcal{P}$ it will be helpful to use quantities

$$\mathcal{Q}_\pm = \mathcal{E} \pm c\mathcal{P}. \qquad (43)$$

The fluxes of $\mathcal{Q}_\pm$ through a surface of $\xi = const$ are

$$F_- = F_{\mathrm{en}} - cF_{\mathrm{mom}} = \frac{c^3\tilde{\rho}h}{\kappa^2}, \qquad (44)$$

$$F_+ = F_{\mathrm{en}} + cF_{\mathrm{mom}} = c^3\tilde{\rho}h - 2cP. \qquad (45)$$

Conservation of $\mathcal{Q}_\pm$ is given by the sum/difference of equations describing energy and momentum conservation (Equation 39) with $\mu = t$ and z):

$$\frac{\partial}{\partial t}\left(T^{tt} \pm T^{tz}\right)\Big|_\xi + \frac{\partial}{\partial\xi}\left(\frac{F_\pm}{c}\right)_t = -\tilde{n}\dot{\mathcal{E}}_e(u_{\mathrm{D}}^t \pm u_{\mathrm{D}}^z). \quad (46)$$

Note that the stress-energy tensor of the radio wave disappears from the conservation law for $\mathcal{Q}_-$. This has

---

[6] This equation can also be derived formally by transforming tensor $T^{\mu\nu}$ to new coordinates: $(t, z) \rightarrow (t, \xi)$. The resulting $T^{t\xi}$ and $T^{z\xi}$ are the energy and momentum fluxes crossing $\xi = const$.

a simple physical reason: the energy and momentum of the wave satisfy $\mathcal{E}_{\mathrm{w}} = c\mathcal{P}_{\mathrm{w}}$, so the wave carries $\mathcal{Q}_- = 0$. There is no exchange of $\mathcal{Q}_-$ in the wave-fluid interaction: whenever the radio wave loses energy $\Delta\mathcal{E}$ to the MHD fluid, it also loses momentum $\Delta\mathcal{P} = \Delta\mathcal{E}/c$, so

$$\Delta\mathcal{Q}_- = \Delta\mathcal{E} - c\,\Delta\mathcal{P} = 0. \tag{47}$$

This observation significantly simplifies the problem. As long as the shape of the propagating radio wave $a(\xi)$ is approximately steady (i.e. the wave is not damped), the fluid dynamics in the packet is fully described by two equations that express conservation of mass and $\mathcal{Q}_-$:

$$\partial_t \rho = -\partial_\xi \left(\frac{\tilde{\rho}}{\kappa} \right), \tag{48}$$

$$\partial_t \left(\frac{\rho h}{\kappa} - \frac{P}{c^2} \right) = -\partial_\xi \left(\frac{\tilde{\rho} h}{\kappa^2} \right) - \frac{\tilde{\rho}}{\kappa}\dot{\gamma}_e. \tag{49}$$

The radio wave does not contribute to these conservation laws, because it carries no mass or $\mathcal{Q}_-$. The wave strength parameter $a(\xi)$ still enters the $\mathcal{Q}_-$ equation through $h = 1 + w + \sigma$ (since a controls the fluid enthalpy w) and through $\dot{\gamma}_e \propto a^2$. As long as $a(\xi)$ is steady, it can be treated as a given function in the wave-fluid interaction problem, so Equations (48) and (49) form a closed set for two unknowns $\rho(t,\xi)$ and $\kappa(t,\xi)$. For a given radio wave packet, the equations can be solved in the domain $0 < \xi < T$ with given initial conditions $\rho(0,\xi)$ and $\kappa(0,\xi)$, and boundary conditions $\rho(t,0) = \rho_{\mathrm{u}}$ and $\kappa(t,0) = \kappa_{\mathrm{u}}$.

Equations (48) and (49) allow one to focus on the fluid dynamics in the wave packet without considering the evolution of the radio wave itself, assuming that the evolution of $a(\xi)$ is negligible on timescales of interest. The consistency of this assumption can be checked later using the remaining independent equation that states conservation of $\mathcal{Q}_+$ and governs the evolution of $a(t,\xi)$. A simpler consistency check can be done by comparing the energy exchanged in the wave-plasma interaction with the wave energy (Section 10).

Note also that Equations (48) and (49) are Lorentz-invariant: they have the same form in any frame boosted along z.[7] They can be solved e.g. in the frame where the upstream plasma is at rest: $\kappa_{\mathrm{u}} = 1$ and $\rho_{\mathrm{u}} = \tilde{\rho}_{\mathrm{u}}$. The problem can also be solved in other frames where $\kappa_{\mathrm{u}} \neq 1$ and the upstream plasma has speed $\beta_{\mathrm{u}} = (\kappa_{\mathrm{u}}^2 - 1)/(\kappa_{\mathrm{u}}^2 + 1)$, Lorentz factor $\gamma_{\mathrm{u}} = (\kappa_{\mathrm{u}}^2 + 1)/2\kappa_{\mathrm{u}}$, and proper density $\tilde{\rho}_{\mathrm{u}} = \rho_{\mathrm{u}}/\gamma_{\mathrm{u}}$.

---

[7] Lorentz transformation of initial conditions is not, however, straightforward, since hypersurfaces of simultaneity ($t = const$) are different in different frames.

5. STEADY COMPRESSION FRONT

The pattern of fluid motion inside the propagating wave packet will be called below the "front" for brevity. Its structure is described by the profiles of $\rho(t,\xi)$ and $\kappa(\xi,t)$, which are governed by Equations (48) and (49). In general, the front structure can evolve in time, as demonstrated in the next section. Here, we first show that there is a unique steady flow pattern, where all quantities depend on ξ only, with no evolution with t. As verified in section 6, the steady state is an attractor for the front evolution. It is reached under two conditions: (1) the front propagation time is long enough for the flow pattern to relax to the steady state, and (2) the propagation time is short enough to neglect damping of the wave, so $a(\xi)$ can be treated as constant in time.

The steady front solution is found by setting $\partial_t|_\xi = 0$ and $\partial_\xi = d/d\xi$ in the MHD equations. Then, Equations (48) and (49) give

$$\frac{d}{d\xi}\left(\frac{\tilde{\rho}}{\kappa} \right) = 0 \quad \Rightarrow \quad \tilde{\rho} = \frac{\kappa}{\kappa_{\mathrm{u}}}\tilde{\rho}_{\mathrm{u}}, \tag{50}$$

$$\frac{d}{d\xi}\left(\frac{h}{\kappa} \right) = -\dot{\gamma}_e. \tag{51}$$

The corresponding lab-frame density $\rho = \gamma_{\mathrm{D}}\tilde{\rho}$ can be expressed using

$$\gamma_{\mathrm{D}} = \frac{\kappa^2 + 1}{2\kappa}, \tag{52}$$

so the solution $\tilde{\rho}/\tilde{\rho}_{\mathrm{u}} = \kappa/\kappa_{\mathrm{u}}$ gives

$$\frac{\rho}{\rho_{\mathrm{u}}} = \frac{1 - \beta_{\mathrm{u}}}{1 - \beta} = \frac{\kappa^2 + 1}{\kappa_{\mathrm{u}}^2 + 1}. \tag{53}$$

The solution $\tilde{\rho}/\rho_{\mathrm{u}} = \kappa/\kappa_{\mathrm{u}}$ also implies $\sigma = \sigma_{\mathrm{u}}\kappa/\kappa_{\mathrm{u}}$ and $d/d\xi(h/\kappa) = d/d\xi[(1 + w)/\kappa]$. Thus, Equation (51) becomes

$$\frac{d}{d\xi}\left(\frac{1 + w}{\kappa} \right) = -\dot{\gamma}_e = -\frac{\sigma_{\mathrm{T}} U}{mc}\frac{\tilde{\gamma}^2}{\kappa^2}. \tag{54}$$

Note that the fluid magnetization σ has dropped out. Remarkably, the fluid motion and compression in a steady front are independent of σ_{u}. In particular, in the case of negligible radiative losses, we find

$$\kappa = (1 + w)\kappa_{\mathrm{u}} \qquad (\text{when } \dot{\gamma}_e = 0), \tag{55}$$

where we used the cold upstream condition $w_{\mathrm{u}} = 0$.

One can also solve for $\kappa(\xi)$ without neglecting radiative losses. In particular, consider the simpler regime of regular heating ($\tilde{\omega}_B < \tilde{\omega}_B$). We are interested in waves with $a \gg 1$, which heat the plasma to $w \approx (3/2)\tilde{\gamma} \gg 1$. Equation (54) can be integrated for $(1 + w)/\kappa$, and we find

$$\kappa = (1 + w)\kappa_{\mathrm{u}}(1 + q), \tag{56}$$

where

$$q(\xi) \approx \frac{4}{9}\frac{\sigma_{\mathrm{T}}\Sigma(\xi)}{mc^2\kappa_{\mathrm{u}}}, \qquad \Sigma(\xi) \equiv \int_0^\xi U(\xi')c\,d\xi'. \tag{57}$$

The importance of radiative losses is controlled by the (Lorentz-invariant) dimensionless parameter q, which is determined by the column energy density of the wave packet, Σ. Equation (55) holds when $q \ll 1$.

6. RELAXATION TO THE STEADY STATE

A simple argument shows that the timescale to approach the steady state is long if the plasma magnetization σ_u is large. Consider the vacuum limit of $\rho_u \to 0$ (which corresponds to $\sigma_u \to \infty$). Then, the background field must remain unchanged from its upstream state: in a vacuum, the electromagnetic wave goes through the background field without interaction, so no E_{bg} is generated. Thus, at $\sigma_u \to \infty$ the magnetized plasma must remain static and will not be compressed by the radio wave packet. The steady-state front with large C still provides a consistent solution, but relaxing to it takes an infinite time, so it becomes irrelevant at $\sigma_u \to \infty$.

A similar conclusion is reached by considering energy. Compression of the magnetically dominated plasma requires deposition of energy $\propto \sigma_u$, much greater than the energy of plasma particles that interact with the wave. The background field serves as a ballast coupled to the plasma. It increases the effective mass per particle from m to $\sigma_u m$, which makes it heavy and impossible to accelerate in the limit of $\sigma_u \to \infty$. An analogy can be drawn with collision of a photon of energy $\mathcal{E}_{ph}$ with a particle of mass σm. Using the frame where the particle is initially at rest, one finds that the particle gains speed $\beta \approx \mathcal{E}_{ph}/\sigma m c^2 \ll 1$ if $\sigma \gg \mathcal{E}_{ph}/mc^2$.

It is worth looking in more detail at a similar collision problem formulated for the wave-plasma system.

6.1. *Wave-plasma collision*

Suppose a radio wave packet of energy $\mathcal{E}$ passes through an initially static, cold slab of plasma with magnetization σ_u. Some energy $\Delta\mathcal{E}$ and momentum $\Delta\mathcal{E}/c$ are lost by the radio wave and received by the slab. As a result, the slab is accelerated to speed β_D and compressed by the factor $1 - \beta_D$ (cf. Equation (53)). Compression increases the slab magnetic field from initial B_u to $B = B_u/(1 - \beta_D)$.

In the simplified collision picture, the slab is treated as a single body characterized by its volume V, particle number N, inertial mass of the plasma $M = Nm(1+w)$ (increased from $M_u = Nm$ by deposited heat), magnetic field B, and electric field $E = \beta_D B$. Energy conservation gives

$$M_u c^2 + V_u \frac{B_u^2}{8\pi} + \Delta\mathcal{E} = \gamma_D M c^2 + V \frac{B^2 + E^2}{8\pi} + \mathcal{E}_{rad}, \quad (58)$$

where we included possible radiative losses of the plasma $\mathcal{E}_{rad}$. The radiated momentum $\mathcal{P}'_{rad} = 0$ in the fluid rest frame implies $\mathcal{P}_{rad} = \beta_D \mathcal{E}_{rad}/c$ in the lab frame. Momentum conservation equation (multiplied by c) is

$$\Delta\mathcal{E} = \gamma_D \beta_D M c^2 + V \frac{EB}{4\pi} + \beta_D \mathcal{E}_{rad}. \quad (59)$$

Subtracting the momentum equation from the energy equation one can exclude $\Delta\mathcal{E}$:

$$M_u c^2 + V_u \frac{B_u^2}{8\pi} = \frac{Mc^2}{\kappa} + V \frac{(B-E)^2}{8\pi} + (1-\beta_D)\mathcal{E}_{rad}. \quad (60)$$

We now substitute $E = \beta_D B$, $B = B_u/(1 - \beta_D)$, $VB = V_u B_u$, and $M = (1+w)M_u$, and obtain

$$1 = \frac{1+w}{\kappa} - \frac{\beta_D \sigma_u}{2} + (1-\beta_D)\epsilon_{rad}, \quad (61)$$

where

$$\sigma_u \equiv \frac{V_u B_u^2}{4\pi M_u c^2}, \qquad \epsilon_{rad} \equiv \frac{\mathcal{E}_{rad}}{M_u c^2}. \quad (62)$$

Radiative losses can be described by the effective scattering cross section σ_{sc} per electron, with $\sigma_{sc} \sim w^2 \sigma_T$ within a factor of ~ 2 (B22). It implies

$$\epsilon_{rad} \sim \frac{\sigma_T w^2 \Sigma}{mc^2}, \quad (63)$$

where Σ is the column energy density of the radio wave packet.

Using the identity $1 - \beta_D = 2/(\kappa^2 + 1)$ one can rewrite Equation (61) as a cubic equation for κ. Its solution simplifies in two limits: $\kappa \gg 1$ ($\beta_D \approx 1$) and $\beta_D \ll 1$ ($\kappa \approx 1$). Assuming $\sigma_u \gg 1$, we find

$$\kappa - 1 \approx \begin{cases} \dfrac{2}{\sigma_u}(w + \epsilon_{rad}) & \text{when } w + \epsilon_{rad} \ll \sigma_u \\[2mm] \dfrac{w}{\sigma_u} + \sqrt{\dfrac{\epsilon_{rad}}{\sigma_u}} & \text{when } w + \epsilon_{rad} \gg \sigma_u \end{cases} \quad (64)$$

It also gives the proper compression factor $\tilde{C} \approx \kappa$.

Once κ is known, we can also find the energy $\Delta\mathcal{E}$ taken from the radio wave packet. Equation (59) gives

$$\frac{\Delta\mathcal{E}}{M_u c^2} = \beta_D \left[\gamma_D(1 + w + \sigma_u \kappa) + \epsilon_{rad} \right], \quad (65)$$

and using Equation (64) we find

$$\frac{\Delta\mathcal{E}}{M_u c^2} \approx \begin{cases} 2(w + \epsilon_{rad}), & w + \epsilon_{rad} \ll \sigma_u \\[2mm] \dfrac{w^2}{\sigma_u} + \dfrac{3}{2}w\sqrt{\dfrac{\epsilon_{rad}}{\sigma_u}} + \dfrac{3}{2}\epsilon_{rad}, & w + \epsilon_{rad} \gg \sigma_u \end{cases} \quad (66)$$

The upstream plasma is composed of many slabs. One after another, they fill the propagating packet and exit behind it, and one might conclude that Equation (64) approximately describes κ in a steady propagating front. In fact, Equation (64) is very far from the correct MHD steady-state solution given in section 5. When viewed in the upstream rest frame, a non-radiative steady front should have $\kappa = 1 + w$ regardless of σ_u (Equation 55). In contrast, the collision model described above yields $\kappa \approx 1 + (2w/\sigma_u) \approx 1$ when $\sigma_u \gg w$.

The simplified collision model (Equation 64) works well at the beginning of packet propagation through the

plasma; however, it fails to describe the gradual relaxation of the compression front to the correct steady state after many interactions with many plasma slabs. When $\sigma_{\rm u} \gg 1$, this relaxation takes a long time and occurs due to a slow growth of magnetic pressure in the front, as demonstrated below. The grown magnetic pressure drops out from the final steady pattern of the MHD flow because it occurs with a zero gradient of σ/κ (section 5). This behavior is not captured by the simplified collision model, which treats each plasma slab passing through the packet as a single body and does not consider any gradients. By contrast, in full MHD, the gradients across the front play an essential role: they endow the propagating front with a "memory" of its earlier interactions with the fluid that has been disposed behind the front. The accumulating memory enables the front relaxation to the steady state.

Below we calculate this relaxation by solving the full time-dependent MHD problem described by Equations (48) and (49). We solve it first in the non-radiative regime (neglecting $\dot{\gamma}_e$ in Equation (49)) and then in the radiative regime. In the remainder of this section, we assume regular heating ($\tilde{\omega}_B > \tilde{\omega}$). A similar relaxation trend holds with stochastic heating ($\tilde{\omega}_B < \tilde{\omega}$); however, this regime gives a huge enthalpy w and relaxation takes a very long time, so steady fronts with stochastic heating are not expected in FRBs (section 9).

6.2. Evolution of a non-radiative compression front

Before solving numerically the time-depending MHD equations, we make a heuristic estimate of the timescale $t_\star$ for the front relaxation toward the steady state.

First, note the time it takes a fluid element to cross the entire wave packet $0 < \xi < T$:

$$t_{\rm cross} = \int_0^T \frac{d\xi}{1 - \beta_{\rm D}} = \int_0^T \frac{\kappa^2 + 1}{2}\, d\xi. \qquad (67)$$

In particular, in a steady state, $\kappa = \kappa_\star \approx 1 + (3/2)a$. Then, for a packet with $a_{\rm max} \gg 1$, one finds

$$t_{\rm cross}^\star \approx \int_0^T \frac{9}{8}\, a^2(\xi)\, d\xi \sim a_{\rm max}^2 T. \qquad (68)$$

Hereafter, star indicates the steady state.

Now consider the momentum per particle carried by the MHD fluid inside the wave packet,

$$\mathcal{P}_{\rm MHD} = \frac{T_{\rm MHD}^{tz}}{nc} = h\gamma_{\rm D}\beta_{\rm D}mc. \qquad (69)$$

It grows when the fluid receives momentum from the wave. Recall that the wave interacts with the plasma particles only, and the plasma shares the received momentum with the background field (through gyration). Therefore, the budget for the wave-fluid momentum exchange (per particle crossing the packet) is set by $T_{\rm p}^{tz}$

rather than $T_{\rm MHD}^{tz}$:

$$\Delta\mathcal{P} = \frac{T_{\rm p}^{tz}}{nc} = (1 + w)\gamma_{\rm D}\beta_{\rm D}mc. \qquad (70)$$

When the fluid flow in the packet is far from the steady state, $\kappa \ll \kappa_\star$, the momentum flux in ξ is non-uniform, $\partial_\xi F_{\rm mom} \neq 0$, and momentum comparable to $\Delta\mathcal{P}$ is retained inside the propagating front $0 < \xi < T$, supporting $(\partial_t\kappa)_\xi > 0$ and $(\partial_t\mathcal{P}_{\rm MHD})_\xi > 0$.

Thus, as long as $\kappa \ll \kappa_\star$, one may expect each particle crossing the wave packet to deposit $\sim \Delta\mathcal{P}$ on the timescale $t_{\rm cross}$ toward future fluid momentum in the propagating front. Then, the timescale to grow $\mathcal{P}_{\rm MHD}$ is

$$t_\mathcal{P} \sim \frac{\mathcal{P}_{\rm MHD}}{\Delta\mathcal{P}}t_{\rm cross} \sim \frac{h}{1 + w}t_{\rm cross}, \qquad (71)$$

where $h = 1 + w + \sigma$. Let us now specialize to the frame where the upstream fluid is at rest ($\kappa_{\rm u} = 1$), and the steady state has $\kappa = \kappa_\star = 1 + w$ and $\sigma = \kappa_\star\sigma_{\rm u} = (1 + w)\sigma_{\rm u}$. In this frame, the expected timescale to approach the steady state is

$$t_\star \sim \frac{1 + w + \kappa_\star\sigma_{\rm u}}{1 + w}\, t_{\rm cross}^\star = (1 + \sigma_{\rm u})t_{\rm cross}^\star \quad (\kappa_{\rm u} = 1). \qquad (72)$$

This simple estimate agrees with our numerical solutions for the front evolution. We find the evolution by solving Equations (48) and (49) for $\kappa(t, \xi)$ and $\rho(t, \xi)$ in a given wave packet $a(\xi)$ propagating in a background plasma with a given upstream magnetization $\sigma_{\rm u}$. The fluid enthalpy inside the packet, $w \equiv (U_{\rm p} + P_{\rm p})/\tilde{\rho}c^2$, is determined by Equations (9) and (20):

$$w(\xi) = \frac{3}{2}\left[\sqrt{a^2(\xi) + 1} - 1\right]. \qquad (73)$$

In sample models, we use the packet described by Equation (5) with $a_{\rm max} = (4/3)\sqrt{7}$ which corresponds to $w_{\rm max} = 4$. As an initial state at $t = 0$, we take a static plasma, $\kappa(\xi) = 1$ and $\rho(\xi) = \rho_{\rm u}$, and follow the evolution of the flow pattern inside the propagating wave packet until it relaxes to the steady-state solution. In the frame where the upstream plasma is at rest ($\kappa_{\rm u} = 1$), the steady-state solution is

$$\kappa_\star = 1 + w, \quad \rho_\star = \frac{\kappa_\star^2 + 1}{2}\rho_{\rm u} \qquad (\kappa_{\rm u} = 1). \qquad (74)$$

The model with $\sigma_{\rm u} = 10$ is shown in Figure 3. At the beginning of the simulation we observe that $\kappa(\xi)$ starts to grow from unity and develops a peaked profile — the MHD fluid is accelerated in the first half of the packet and decelerated in the second half, before exiting behind the packet. Over time, $\kappa(\xi)$ approaches $\kappa_\star(\xi)$, which is an attractor for the flow pattern. In particular, the maximum of the κ-profile, $\kappa_{\rm max}$, eventually approaches the expected $\kappa_{\rm max}^\star = 1 + w_{\rm max} = 5$. The maximum compression factor $C_{\rm max} = \rho_{\rm max}/\rho$ approaches

$$C_{\rm max}^\star = \frac{1}{2}\left[(1 + w_{\rm max})^2 + 1\right]. \qquad (75)$$
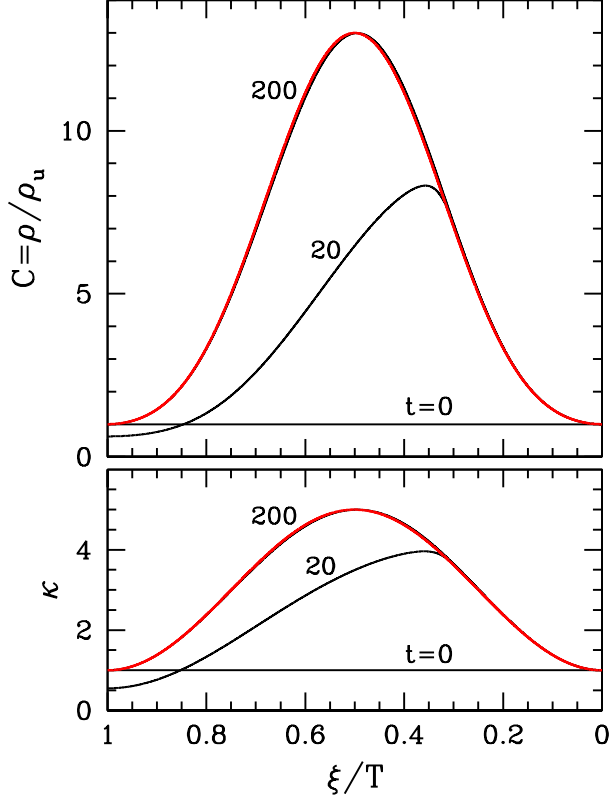
Figure 3. Top: relaxation of the non-radiative compression front $C(\xi)$ toward the steady-state $C_\star(\xi)$ (red curve, Equation (74)) from an initial state with a uniform static plasma, $C = 1$ and $\kappa = 1$. Black curves show snapshots of the front, with time t indicated next to each curve (in units of packet duration T). The wave packet (Equation 5) has $a_{\max} = (4/3)\sqrt{7}$, equivalent to $w_{\max} = 4$. The upstream magnetization is $\sigma_{\mathrm{u}} = 10$. Bottom: evolution of κ from the initial $\kappa = 1$ toward $\kappa_\star$ in the same simulation.

The evolution of compression peak $C_{\max}(t)$ provides a simple way to quantify the front relaxation toward the steady-state. The evolution of $C_{\max}$ is shown in Figure 4 for $\sigma_{\mathrm{u}} = 3, 10, 20$. One can see that the timescale $t_\star$ for approaching the steady-state $C^\star_{\max} = 13$ increases with σ_{u} in agreement with Equation (72). The slow evolution occurs through a sequence of quasi-steady states with a nearly uniform mass flux in ξ, $F_{\mathrm{m}} = \rho(c-v) \approx const$. It implies a correlated growth of κ and C: the relation $C \approx (\kappa^2 + 1)/2$ is sustained during the evolution (Figure 5).

We conclude that at any large but finite σ_{u}, the wave packet approaches the steady state on a long timescale $t_\star \sim \sigma_{\mathrm{u}} t_{\mathrm{cross}}$ (assuming negligible damping of the radio wave during this time). The conclusion might seem counter-intuitive: one might expect that the front has no memory on timescales longer than t_{cross} since the plasma interacting with the wave packet is continually refreshed on the timescale t_{cross}. Nevertheless, the conservation
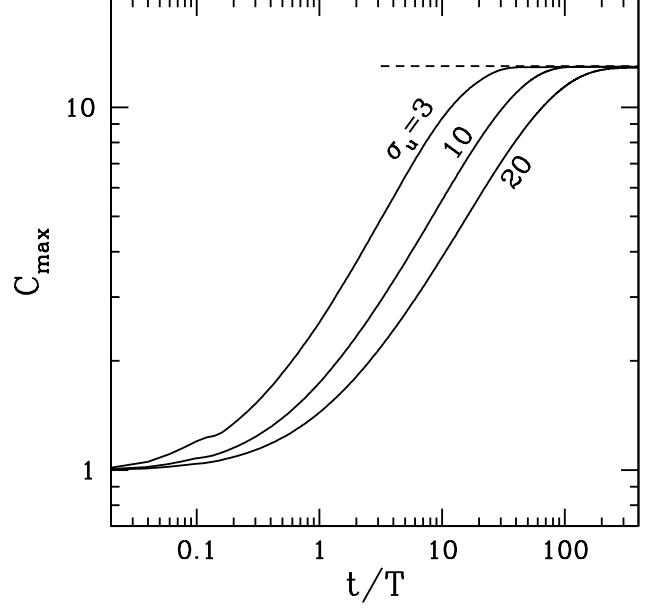

Figure 4. Evolution of the compression peak $C_{\max}$ from the initial $C_{\max} = 1$ to the steady-state $C^\star_{\max} = 13$ (indicated by the horizontal dashed line) for the non-radiative fronts with $\sigma_{\mathrm{u}} = 3, 10$, and 20.

laws require the propagating wave to retain some memory of its previous interactions with the plasma. Given enough time, the packet gradually builds up the strong compression $\tilde{\rho}/\rho_{\mathrm{u}} = \kappa \approx w$ — the pattern of the MHD flow in the wave is "groomed" toward the steady state. Remarkably, this gradual evolution leads to a strong magnetic field in the packet, so that the plasma magnetization approaches $\sigma \approx w\sigma_{\mathrm{u}}$. Thus, tremendous magnetic pressure develops in the propagating front while it finds a self-consistent steady pattern. At the same time, the final pattern of fluid motion established in the wave packet is the same as it would be in the absence of magnetic pressure, as the background magnetic field drops out from the steady-state solution $\kappa_\star(\xi)$.

6.3. *Evolution of a radiative compression front*

In the regime of $q \gg 1$, the fluid element moving through the wave packet experiences strong radiative losses. The radio wave sustains the fluid enthalpy $w \approx (3/2)a$ by continually depositing energy to offset the losses (B22). Thus, the received power per particle (measured in the local fluid frame) equals the emitted power $\dot{\mathcal{E}}_e$ (Lorentz invariant). The wave-fluid interaction is basically a scattering process with the cross section $\sigma_{\mathrm{sc}} = \dot{\mathcal{E}}_e/F$, where $F = cU$ is the energy flux of the radio wave.

The scattering is accompanied by a radiative pressure force $\dot{\mathcal{P}}$, which is Lorentz-invariant and easiest to find in
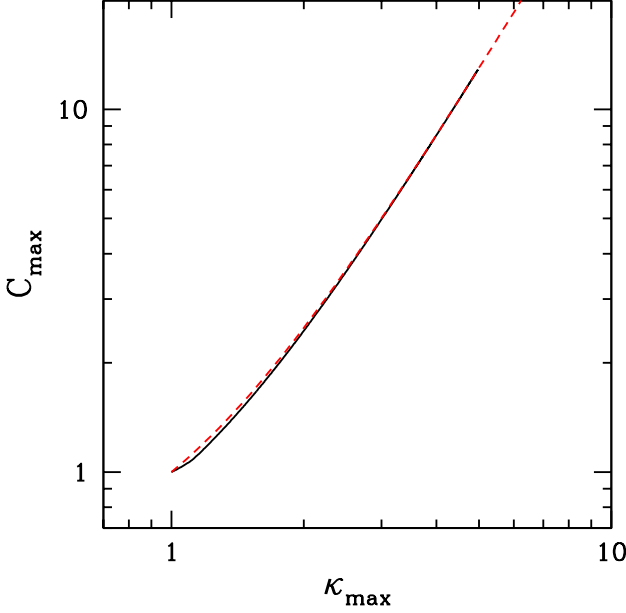
Figure 5. Relation between $\kappa = \gamma_{\rm D}(1 + \beta_{\rm D})$ and $C = \rho/\rho_{\rm u}$ (here measured at the peak inside the compression front) during relaxation toward the final steady state. Black curve shows the simulation result (the model with $\sigma_{\rm u} = 20$), and red dashed curve shows the relation $C = (\kappa^2 + 1)/2$, equivalent to $\tilde{\rho}/\kappa = \rho_{\rm u}$ (a uniform mass flux in ξ, $F_{\rm m} = \rho(c - v)$). Fluid density in the front closely tracks the steady-state solution $\tilde{\rho} = \kappa\rho_{\rm u}$ defined for an instantaneous profile of $\kappa(\xi)$, which slowly grows during relaxation. The correlated growth of κ and C stops when they reach $\kappa_{\rm max} = 5$ and $C_{\rm max} = 13$. Then, the fluxes $F_{\rm m}$ and F_- both become exactly uniform across the front, and a true steady state is achieved.

the local fluid frame where $\dot{\mathcal{P}} = \dot{\mathcal{E}}_e/c$, so

$$\dot{\mathcal{P}} = \frac{\dot{\mathcal{E}}_e}{c} = \sigma_{\rm T}\tilde{U}\,\tilde{\gamma}^2 = \frac{\sigma_{\rm T}U}{\kappa^2}\,\tilde{\gamma}^2. \tag{76}$$

A fluid element crossing the front gains from scattering the following net momentum per particle:

$$\Delta\mathcal{P}_{\rm sc} = \int_0^{t_{\rm cross}} \dot{\mathcal{P}}\,dt = \int_0^T \frac{\dot{\mathcal{P}}\,d\xi}{1 - \beta_{\rm D}}$$
$$\sim \left(1 + \frac{1}{\kappa^2}\right)\sigma_{\rm T}U a^2 T, \tag{77}$$

with $a \sim a_{\rm max}$. This sets the budget for the fluid momentum exchange with the wave per crossing time $t_{\rm cross}$. The gained momentum is shared with the magnetic field frozen in the fluid, increasing $\mathcal{P}_{\rm MHD}$.

Similarly to the non-radiative case, one can make a heuristic timescale estimate for the growth of $\mathcal{P}_{\rm MHD}$ in the frame where the upstream plasma is at rest ($\kappa_{\rm u} = 1$):

$$t_{\mathcal{P}} \sim \frac{\mathcal{P}_{\rm MHD}}{\Delta\mathcal{P}_{\rm sc}}\,t_{\rm cross} \sim \frac{h\kappa}{qw^2}\,t_{\rm cross}, \tag{78}$$

where q is evaluated using the entire column energy of the wave packet $\Sigma(T)$ (Equation 57). Equation (78) gives the timescale for approaching the steady state, $t_\star = t_{\mathcal{P}}(\kappa_\star)$ if we substitute $\kappa \sim \kappa_\star \approx qw$ (Equation 56) and $h_\star = 1 + w + \kappa_\star\sigma_{\rm u} \approx \kappa_\star\sigma_{\rm u}$:

$$t_\star \sim q\,\sigma_{\rm u}t_{\rm cross} \qquad (q \gg 1,\ \sigma_{\rm u} \gg 1). \tag{79}$$

This estimate may be compared with the results of numerical simulations presented below.

Front relaxation to the steady state in the radiative regime is found by solving Equations (48) and (49) similarly to section 6.2, but now keeping the term $\dot{\gamma}_e \neq 0$. This term may be expressed as follows

$$\dot{\gamma}_e = \mathcal{R}\frac{w^4}{\kappa^2} \quad (w \gg 1), \qquad \mathcal{R} \equiv \left(\frac{2}{3}\right)^5 \frac{r_e}{c}\,\omega^2. \tag{80}$$

The value of $\mathcal{R}$ depends on the choice of a reference frame, which can be parameterized by the upstream motion $\beta_{\rm u}$ or $\kappa_{\rm u}$. Note that $\kappa_{\rm u} < 1$ ($\beta_{\rm u} < 0$) in frames moving in the $+z$ direction relative to the upstream plasma. The wave frequency ω in a chosen frame scales as $\omega \propto \kappa_{\rm u}$, so $\mathcal{R} \propto \kappa_{\rm u}^2$. Note also that the packet width T depends on the choice of a frame as $\kappa_{\rm u}^{-1}$ (since $\omega T = inv$), and the radiative parameter $q \propto T\mathcal{R}/\kappa_{\rm u}$ is invariant.

We use the following technical tricks to avoid two complications:

(1) Radiative losses $\dot{\gamma}_e$ may be important only when $w \gg 1$ because of the small value of $\mathcal{R}$ for real FRBs. We avoid simulating huge w and κ by rescaling $\mathcal{R}$ to larger values, so that we can experiment with the radiative regime $q \gg 1$ at moderate w and κ accessible to simulations. In sample models, we use the wave packet described by Equation (5) with $a_{\rm max} = (4/3)\sqrt{7}$ (which gives $w_{\rm max} = 4$) and set the invariant radiative parameter $T\mathcal{R}/\kappa_{\rm u} = 1$. This choice gives $q \sim 3$.

(2) Both κ and ρ grow by a large factor during relaxation toward the steady state. The simulation is more efficient if performed in a boosted frame where $\kappa_{\rm u} \ll 1$. This helps avoid ultra-relativistic motions of the accelerated fluid along the wave propagation direction (large $\kappa \gg 1$) that would slow down the simulation. We use the frame where $\kappa_{\rm u} = 0.05$. When presenting the results, we transform the fluid parameters to the upstream rest frame (where $\kappa_{\rm u} = 1$), so figures will show κ and $C = \rho/\rho_{\rm u}$ measured in the upstream frame.

As an initial condition at $t = 0$, we take the MHD fluid in the non-radiative steady front. In the rest frame of the upstream plasma, it is given by $\kappa_0(\xi) = 1 + w(\xi)$ and $C_0(\xi) = (\kappa_0^2 + 1)/2$. In particular, the initial compression peak is $C_{\rm max}(0) = 13$. In the presence of radiative losses, this flow pattern is no longer a steady state, so it immediately begins to evolve at $t > 0$. Both κ and C grow and eventually relax to a new steady state.

Figure 6 shows the evolution of $C_{\rm max}$, and Figure 7 shows the final profiles of $\kappa(\xi)$ and $C(\xi)$. The relaxation
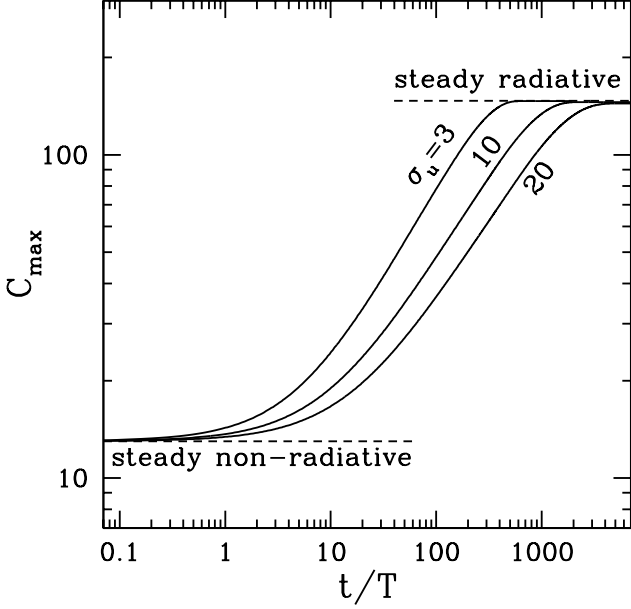
Figure 6. Evolution of the compression peak $C_{\max}$ from the non-radiative steady state ($C_{\max} = C^\star_{\max} = 13$ at $t = 0$) after switching on radiative losses with $T\mathcal{R}/\kappa_{\mathrm{u}} = 1$ (the radiative parameter $\mathcal{R}$ is defined in Equation (80)). The front evolves toward the new steady state with $C^\star_{\max} \approx 147$. The evolution is shown for three simulations with upstream magnetizations $\sigma_{\mathrm{u}} = 3, 10, 20$. The initial and final states are independent of σ_{u} and shown in Figure 7.

is determined by the chosen radiative coefficient $\mathcal{R}$ and the corresponding $q \sim 3$. In particular, $\kappa_{\max}$ grows from its initial value $1 + w_{\max} = 5$ to the final value $\kappa_{\max} = 17$, consistent with the factor of $q \sim 3$, and $C_{\max}$ grows from 13 to 147, confirming the expected increase $\sim q^2$.

The simulations also confirm the expected scaling of the relaxation timescale $t_\star \propto q\sigma_{\mathrm{u}}$ at $q \gg 1$ and $\sigma_{\mathrm{u}} \gg 1$ (Equation 79). This scaling can be seen in Figure 6, which shows three models with $\sigma_{\mathrm{u}} = 3, 10,$ and 20. Note that $t_{\mathrm{cross}} \propto \kappa^2 \propto q^2 w^2$, and hence $t_\star$ should scale as q^3 at $q \gg 1$. One can see that the relaxation timescale is indeed increased by a large factor $\sim q^3 \sim 30$ compared with the non-radiative front evolution shown in Figure 4.

As expected, the final steady state is independent of σ_{u}: it is the same in all three simulations with $\sigma_{\mathrm{u}} = 3, 10, 20$. The steady-state profiles of $\kappa(\xi)$ and $C(\xi)$ are shown in Figure 7 and agree with Equation (56). Note that in the non-radiative regime ($q \ll 1$) the fluid comes back to rest as it exits behind the wave packet. In contrast, the fluid behind the radiative front has a large speed $\beta_{\mathrm{D}} > 0$ ($\kappa \gg 1$). This is a consequence of momentum deposition by scattering during the fluid motion through the wave packet.
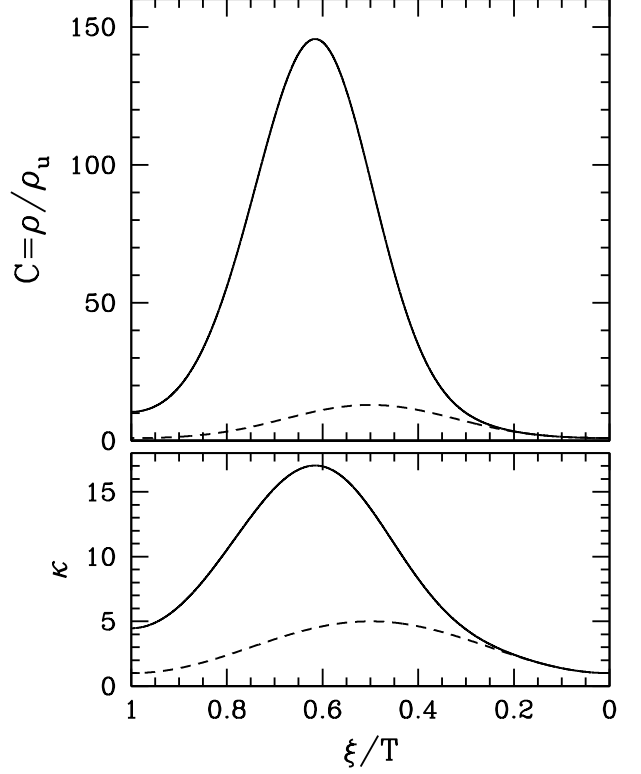

Figure 7. The initial and final profiles of the compression front in the three simulations shown in Figure 6. The initial state is the steady non-radiative front (Figure 3, red curve); here it is shown by the black dashed curve. Radiative losses make the front evolve until it reaches a new steady state (solid curve), which reproduces the solution in Equation (56).

7. PARAMETERS OF THE WIND

The obtained picture of a radio wave interaction with MHD fluid can now be applied to FRBs propagating through a radial wind. The wind serves as the upstream medium for the wave packet, and we begin with a brief summary of its parameters. They are denoted with subscript "u" for consistency of notation in this paper.

The wind Lorentz factor γ_{u} and magnetization σ_{u} are estimated in Beloborodov (2020) (denoted there as Γ_{w} and σ_{w}). Their typical values are $\sigma_{\mathrm{u}} \sim 10^2 - 10^3$ and $\gamma_{\mathrm{u}} \sim 10 - 30$ at radii $r \gtrsim 10^{11}$ cm. The wind is also characterized by the particle outflow rate $\dot{\mathcal{N}}$ and power L_{w}, which is dominated by the Poynting flux. Its isotropic equivalent (power per unit solid angle multiplied by 4π) is

$$L_{\mathrm{w}} \approx cr^2 B_{\mathrm{u}}^2 = \eta mc^2 \dot{\mathcal{N}}, \qquad \eta = \sigma_{\mathrm{u}}\gamma_{\mathrm{u}}. \qquad (81)$$

A spinning magnetar emits a spindown wind with power

$$L_{\mathrm{w}} \approx \frac{\mu^2 \Omega^4}{c^3} \approx 5.8 \times 10^{37} \, \mu_{33}^2 P^{-4} \, \mathrm{erg\,s^{-1}}, \qquad (82)$$

where μ is the magnetic dipole of the magnetar and $P = 2\pi/\Omega$ is its rotation period (in seconds). The spin-

down power gives a lower bound on $L_{\rm w}$, which can be enhanced during magnetar activity.

The wind forms at the light cylinder $R_{\rm LC} = c/\Omega$ and its Lorentz factor grows as $\gamma_{\rm u}(r) \approx r/R_{\rm LC}$ until it reaches $\eta^{1/3}$; at larger radii, $\gamma_{\rm u}$ grows logarithmically (Lyubarsky & Kirk 2001). We will use a simple approximation:

$$\gamma_{\rm u} \approx \begin{cases} \dfrac{r}{R_{\rm LC}} & r < \eta^{1/3} R_{\rm LC} \\[2ex] \left[\dfrac{\eta}{\ln 2} \ln\left(1 + \dfrac{r}{\eta^{1/3} R_{\rm LC}} \right) \right]^{1/3} & r > \eta^{1/3} R_{\rm LC} \end{cases} \tag{83}$$

Our description of the wind is imprecise at small radii $r \sim R_{\rm LC}$ for two reasons. (1) The wind magnetic field is assumed to be transverse to the radial direction. In fact, it has a radial component B_r (which quickly decreases at $r > R_{\rm LC}$). (2) The wind speed is taken equal to the drift speed. This approximation would be strongly violated for ordinary radio pulsars, where plasma outflows at $R_{\rm LC}$ with a high Lorentz factor; however, it is reasonable for magnetars whose radiation field makes the outflow mildly relativistic (Beloborodov 2020). Our wind description should hold outside a few $R_{\rm LC}$.

The parameter $\eta = \sigma_{\rm u}\gamma_{\rm u}$ equals the plasma magnetization at the light cylinder,

$$\eta = \sigma_{\rm LC} \sim \frac{\mu^2}{4\pi R_{\rm LC}^3 \mathcal{N} mc^2} \approx 10^4 \frac{\mu_{33}^2}{R_{\rm LC,10}^3 \mathcal{N}_{37}}, \tag{84}$$

where $\mathcal{N} \equiv nr^3$ is the density parameter of the magnetosphere; its typical value is $\mathcal{N} \sim 10^{37}$ (Beloborodov 2020). The parameter η and the Lorentz factor $\gamma_{\rm u}(r)$ determine the wind magnetization $\sigma_{\rm u}(r) = \eta/\gamma_{\rm u}$.

Note that $L_{\rm w}$ determines the wind magnetic field in the static lab frame $B_{\rm u}(r)$ according to Equation (81). The corresponding magnetic field in the rest frame of the wind (ahead of the FRB wave packet) is $\tilde{B} = B_{\rm u}/\gamma_{\rm u}$. It sets another important parameter — the gyro-frequency of the wind plasma,

$$\tilde{\omega}_B^{\rm u} = \frac{e\tilde{B}_{\rm u}}{mc} = \frac{e}{\gamma_{\rm u} mcr} \left(\frac{L_{\rm w}}{c} \right)^{1/2}, \tag{85}$$

which should be compared with the FRB frequency. When viewed in the wind rest frame, the FRB frequency ω is redshifted to $\tilde{\omega}_{\rm u} = \omega/\kappa_{\rm u}$ where $\kappa_{\rm u} \equiv \gamma_{\rm u}(1 + \beta_{\rm u}) \approx 2\gamma_{\rm u}$. Then, we find

$$\alpha \equiv \frac{\tilde{\omega}_B^{\rm u}}{\tilde{\omega}_{\rm u}} \approx \frac{2e}{mcr\omega} \left(\frac{L_{\rm w}}{c} \right)^{1/2} \approx 0.1 \frac{L_{\rm w,37}^{1/2}}{\nu_9 r_{12}}. \tag{86}$$

Below we examine the compression front driven by an FRB emitted at some radius r and propagating outward through the wind. We first describe the front at large r, where FRBs induce heating in the regular regime ($\tilde{\omega}_B < \tilde{\omega}$), and then consider FRBs emitted at smaller r, where heating is stochastic and more dramatic effects occur, including damping of the FRB.

8. REGULAR HEATING ZONE

Strong compression is expected at radii where the FRB has $a > 1$. The wave strength parameter a (Equation 1) may be written as $a = r_1/r$, where

$$r_1 = \left(\frac{r_e L}{mc\omega^2} \right)^{1/2} \approx 1.6 \times 10^{13} L_{42}^{1/2} \nu_9^{-1} \, {\rm cm}. \tag{87}$$

8.1. Saturated compression ($r > r_\star$)

One can quickly formulate a compression front model using the steady-state solution described by Equations (50), (55), and (73), assuming the regular heating regime ($\tilde{\omega}_B < \tilde{\omega}$) and neglecting radiative losses. Using the definition of the proper compression factor $\tilde{C} \equiv \tilde{\rho}/\tilde{\rho}_{\rm u}$, the steady front solution can be stated as

$$\tilde{C}_\star = \frac{\kappa_\star}{\kappa_{\rm u}} = 1 + \frac{3}{2} \left(\sqrt{a^2 + 1} - 1 \right). \tag{88}$$

The corresponding compression factor for the wind density measured in the lab frame, $C \equiv \rho/\rho_{\rm u}$, is

$$C_\star = \frac{\kappa_\star^2 + 1}{\kappa_{\rm u}^2 + 1} \approx \tilde{C}_\star^2, \tag{89}$$

where $\kappa \equiv \gamma_{\rm D}(1 + \beta_{\rm D})$ describes the fluid drift speed $\beta_{\rm D}$, and we used $\kappa_{\rm u} \gg 1$ since the upstream medium is a relativistic wind. Outside the radius r_1 (where $a \ll 1$), one finds weak compression $C_\star \approx 1$ while inside r_1 (where $a \gg 1$) one finds $C_\star \approx (9/4)a^2 = (9/8)a_0^2 \approx a_0^2$. A simple approximate expression matching the two cases is

$$C_\star \approx 1 + a_0^2. \tag{90}$$

Remarkably, this compression is consistent with the results of Sobacchi et al. (2024), who investigated a steady plasma flow in a (nearly monochromatic) wave packet using a different technique.

However, the simple solution stated in Equation (90) does not correctly describe compression fronts in FRBs at small radii $r \ll r_1$, for two reasons:

(1) At $r < r_\star$ defined below, the compression front does not reach the steady state, so the actual compression factor is well below its saturated value, $C \ll C_\star$.

(2) Compression promotes the transition to stochastic acceleration of plasma particles in the FRB wave packet. The plasma then experiences much stronger heating, and the momentum exchange between the FRB wave packet and the plasma is enhanced, changing κ and C.

These two features qualitatively change the picture of the FRB compression front, as described below.

8.2. Unsaturated compression ($r < r_\star$)

The saturated (steady-state) compression factor $C_\star$ may be reached only when the wave packet has propagated for a time $t > t_\star$. In the regular heating regime ($\tilde{\omega}_B < \tilde{\omega}_B$), the timescale $t_\star$ is given by Equation (72)

in the frame where the upstream plasma is at rest ($\kappa_\mathrm{u} = 1$). The corresponding timescale measured in any other frame (any κ_u) is $t_\star \sim \sigma_\mathrm{u} a^2 \gamma_\mathrm{u}^2 T$ (assuming $a^2 > 1$). So, the relaxation timescale in our static lab frame is

$$t_\star \sim \eta \gamma_\mathrm{u} a^2 T. \tag{91}$$

Comparing $t_\star$ with the propagation time $t = r/c$ and using $\gamma_\mathrm{u} \approx \eta^{1/3}$ at $r \gtrsim \eta^{1/3} R_\mathrm{LC}$, we find

$$\frac{t}{t_\star} = \frac{r^3}{r_\star^3}, \tag{92}$$

$$r_\star \approx \left(\frac{r_e \mathcal{E} \eta \gamma_\mathrm{u}}{m \omega^2} \right)^{1/3} \approx 10^{13} \frac{\mathcal{E}_{39}^{1/3} \eta_4^{4/9}}{\nu_9^{1/3}} \, \mathrm{cm}, \tag{93}$$

where $\mathcal{E} \sim LT$ is the FRB energy. This expression for $r_\star$ assumes $a^2(r_\star) > 1$, i.e. it holds as long as $r_\star < r_1$. At the transition radius $r = r_\star$ we find

$$C(r_\star) \approx C_\star(r_\star) \approx \left[1 + \frac{3}{2} \left(\sqrt{\frac{r_1^2}{r_\star^2} + 1} - 1 \right) \right]^2. \tag{94}$$

When $t_\star > t = r/c$, the propagating wave packet develops compression factors $C < C_\star$ (Figure 4). At times $\gamma_\mathrm{u}^2 T \ll t \ll t_\star$, $C(t)$ may be approximated by

$$C - 1 \approx (C_\star - 1) \left(\frac{t}{t_\star} \right)^\zeta \approx \frac{9}{4} a^2 \left(\frac{r}{\eta \gamma_\mathrm{u} a^2 cT} \right)^\zeta. \tag{95}$$

The numerical results in Figure 4 suggest $\zeta \approx 1/2$.

9. STOCHASTIC HEATING ZONE

The zone of stochastic heating ($\tilde{\omega}_B > \tilde{\omega}$) is larger than one might expect from the ratio $\tilde{\omega}_B^\mathrm{u}/\tilde{\omega}_\mathrm{u}$ (Equation 86). Even when $\tilde{\omega}_B < \tilde{\omega}$ in the upstream plasma, the condition $\tilde{\omega}_B > \tilde{\omega}$ can be met inside the wave packet as a result of the fluid acceleration and compression: acceleration reduces $\tilde{\omega}$ and compression increases $\tilde{\omega}_B$.

Fluid acceleration (κ/κ_u) and compression ($\tilde{C}$ or C) are related by

$$\tilde{C} \equiv \frac{\tilde{\rho}}{\tilde{\rho}_\mathrm{u}} \approx \frac{\kappa}{\kappa_\mathrm{u}}, \qquad C \equiv \frac{\rho}{\rho_\mathrm{u}} \approx \frac{\kappa^2 + 1}{\kappa_\mathrm{u}^2 + 1}. \tag{96}$$

These relations are exact for a steady compression front (with $C = C_\star$ and $\kappa = \kappa_\star$) and also approximately hold for unsaturated compression ($C \ll C_\star$ and $\kappa \ll \kappa_\star$), as demonstrated in Figure 5 using the frame where the upstream plasma is at rest ($\kappa_\mathrm{u} = 1$). Equation (96) states the κ-C relation viewed in any reference frame, where κ_u can have any value. The magnetic field is frozen in the fluid and compressed by the same factor as density:

$$\frac{\tilde{B}}{\tilde{B}_\mathrm{u}} = \tilde{C}, \qquad \frac{B}{B_\mathrm{u}} = C, \tag{97}$$

where $\tilde{B}$ is measured in the local fluid rest frame, and subscript "u" indicates the upstream region ahead of the FRB. Equation (97) implies

$$\tilde{\omega}_B \approx \frac{\kappa}{\kappa_\mathrm{u}} \tilde{\omega}_B^\mathrm{u}. \tag{98}$$

The FRB frequency ω transforms to the local fluid frame as $\tilde{\omega} = \omega/\kappa$. Hence,

$$\frac{\tilde{\omega}_B}{\tilde{\omega}} \approx \frac{\kappa^2}{\kappa_\mathrm{u}^2} \frac{\tilde{\omega}_B^\mathrm{u}}{\tilde{\omega}_\mathrm{u}}. \tag{99}$$

In the lab frame, the upstream medium (the wind) moves with $\kappa_\mathrm{u} \approx 2\gamma_\mathrm{u} \gg 1$, and Equation (99) may be re-written as

$$\frac{\tilde{\omega}_B}{\tilde{\omega}} \approx C \frac{\tilde{\omega}_B^\mathrm{u}}{\tilde{\omega}_\mathrm{u}} = C\alpha. \tag{100}$$

Now using Equation (86) one can see that $\tilde{\omega}_B > \tilde{\omega}$ when

$$C > C_\mathrm{stoch} \approx \frac{\tilde{\omega}_\mathrm{u}}{\tilde{\omega}_B^\mathrm{u}} \approx 10 \frac{r_{12} \nu_9}{L_\mathrm{w,37}}. \tag{101}$$

The stochastic regime $\tilde{\omega}_B > \tilde{\omega}$ appears at $r < r_\mathrm{stoch}$, with the transition radius r_stoch typically inside $r_\star$. Its value is found by equating C given by Equation (95) to C_stoch. In particular, for $\zeta \approx 1/2$ we find

$$r_\mathrm{stoch} \approx \left(\frac{4 r_e^2 L_\mathrm{w} L}{m^2 c^3 \omega^4 \eta \gamma_\mathrm{u} T} \right)^{1/3}. \tag{102}$$

This gives $r_\mathrm{stoch} \sim 10^{12} \, \mathrm{cm}$ for typical parameters. When $r_\mathrm{stoch} > \eta^{1/3} R_\mathrm{LC}$, one can substitute $\gamma_\mathrm{u} \approx \eta^{1/3}$ and then Equation (102) implies $r_\mathrm{stoch} \propto L^{1/3}$. If one keeps ζ as a parameter that may differ from $1/2$, one still finds $r_\mathrm{stoch} \propto L^{1/3}$:

$$r_\mathrm{stoch} \approx 7 \times 10^{11} \, H \, L_{42}^{1/3} \, \mathrm{cm}, \tag{103}$$

$$H \approx \left(\frac{L_\mathrm{w,37}^{1/2}}{T_\mathrm{ms}^\zeta \eta_4^{4\zeta/3} \nu_9^{3-2\zeta}} \right)^{1/(3-3\zeta)}. \tag{104}$$

The expression for H omits a ζ-dependent prefactor, which deviates from unity when ζ deviates from $1/2$.

9.1. Heating and radiative cooling in the wave packet

At radii $r < r_\mathrm{stoch}$, the FRB stochastically heats plasma particles to $\tilde{\gamma} \gg a$, far exceeding regular heating. In this regime, $\tilde{\gamma}$ monotonically grows in the fluid element as it crosses the wave packet (Figure 2). The growth is well described by Equation (18) with the numerical coefficient $\chi \approx 2/3$. It was derived in the frame where the upstream plasma is at rest ($\kappa_\mathrm{u} = 1$), and a similar derivation can be repeated in any frame with $\kappa_\mathrm{u} \neq 1$ (the only change occurs in the expression for the gyro-frequency $\tilde{\omega}_B = \tilde{\omega}_B^\mathrm{u} \kappa/\kappa_\mathrm{u}$ (Equation 98)). Thus, we find

$$\tilde{\gamma}^{4/3} \frac{d\tilde{\gamma}}{d\xi} \approx \frac{16\pi}{3} \frac{r_e U \kappa^{2/3}}{m \omega^{4/3}} \left(\frac{\tilde{\omega}_B^\mathrm{u}}{\kappa_\mathrm{u}} \right)^{1/3}, \tag{105}$$

where we substituted $a^2 = 4\pi r_e U/m\omega^2$. Integration for $\tilde{\gamma}(\xi)$ then gives

$$\tilde{\gamma}_{\text{stoch}} \approx \left[\frac{3r_e\mathcal{E}}{mc\omega r^2}\right]^{3/7}(C\alpha)^{1/7} \approx 10^5 \frac{\mathcal{E}_{39}^{3/7}C^{1/7}L_{\text{w},37}^{1/14}}{\nu_9^{4/7}r_{11}}, \tag{106}$$

where $\mathcal{E} = 4\pi r^2\Sigma = \int 4\pi r^2 Uc\,d\xi$ is the energy of the radio wave (isotropic equivalent). Stochastic heating is stronger than the regular heating by a factor of $\sim 10^3$.

Equation (106) holds as long as radiative losses of the plasma are negligible. The losses $\dot{\gamma}_e$ are given by Equation (34) (with the coefficient 2/3 replaced by 4/3 for stochastically heated particles, see B22). Losses $\dot{\gamma}_e$ offset the heating rate (Equation 10) when $\tilde{\gamma}$ approaches $\tilde{\gamma}_{\text{rad}} = (c/r_e)^{3/10}\tilde{\omega}_B^{1/10}\tilde{\omega}^{-2/5}$. Using $\tilde{\omega} = \omega/\kappa = \tilde{\omega}_{\text{u}}\kappa_{\text{u}}/\kappa$ and $\tilde{\omega}_B = \tilde{\omega}_B^{\text{u}}\kappa/\kappa_{\text{u}}$, we find

$$\tilde{\gamma}_{\text{rad}} \approx \left(\frac{c}{r_e\omega}\right)^{0.3}\alpha^{0.1}\frac{\kappa^{0.5}}{\kappa_{\text{u}}^{0.2}} \approx 10^4\frac{C^{1/4}\kappa_{\text{u}}^{0.3}L_{\text{w},37}^{1/20}}{\nu_9^{0.4}r_{11}^{0.1}}. \tag{107}$$

In summary, stochastic heating gives

$$\tilde{\gamma} = \min\{\tilde{\gamma}_{\text{stoch}}, \tilde{\gamma}_{\text{rad}}\}. \tag{108}$$

The radiative regime $\tilde{\gamma} = \tilde{\gamma}_{\text{rad}}$ occurs at radii that satisfy

$$r < \frac{6 \times 10^{11}}{\gamma_{\text{u}}^{1/3}}\frac{\mathcal{E}_{39}^{10/21}L_{\text{w},37}^{1/42}}{C_2^{5/42}\nu_9^{4/21}}\text{ cm}. \tag{109}$$

9.2. Plasma compression and trapping by the FRB

Once the radio wave begins to propagate through the plasma, it immediately induces significant compression C (section 6.1), which will be denoted below as C_0. When propagation occurs in the zone of stochastic heating $r < r_{\text{stoch}}$, the immediate compression C_0 turns out so large that further growth of $C > C_0$ on timescales $t \gg t_{\text{cross}}$ (front relaxation toward the steady state) is irrelevant, because t_{cross} becomes too long. In general, large C corresponds to large $\gamma_{\text{D}} \approx C^{1/2}\gamma_{\text{u}}$ and implies a long timescale for the plasma to cross the wave packet $t_{\text{cross}} \sim \gamma_{\text{D}}^2 T$ (Equation 67). When t_{cross} reaches $t = r/c$, the plasma becomes trapped in the packet, surfing the radio wave. The ratio t/t_{cross} may be written as

$$\frac{t_{\text{cross}}}{t} \sim \frac{cT\gamma_{\text{D}}^2}{r} = \frac{\gamma_{\text{D}}^2}{\gamma_{\text{trap}}^2} = \frac{C}{C_{\text{trap}}}, \tag{110}$$

where

$$\gamma_{\text{trap}} \approx \left(\frac{r}{cT}\right)^{1/2}, \qquad C_{\text{trap}} \approx \frac{r}{cT\gamma_{\text{u}}^2}. \tag{111}$$

Let us now evaluate the compression factor C_0 that immediately develops in the FRB-wind interaction, and show that it easily reaches C_{trap}. The calculation was set up in section 6.1 using the frame where the upstream plasma is at rest. Here, we will denote this frame $\mathcal{K}'$ to distinguish it from our lab frame; quantities measured in frame $\mathcal{K}'$ will be denoted with a prime. We are interested in the strong compression regime $\tilde{C}_0 \gg 1$. Then, Equation (64) gives

$$\tilde{C}_0 \approx \kappa' \approx \frac{3\tilde{\gamma}}{2\sigma_{\text{u}}} + \sqrt{\frac{\epsilon_{\text{rad}}'}{\sigma_{\text{u}}}}, \tag{112}$$

where we used $w \approx (3/2)\tilde{\gamma}$.

A proper compression factor $\tilde{C}$ corresponds to $C \approx \tilde{C}^2$ in the lab frame (Equation 96), and radiative losses in the lab frame are $\mathcal{E}_{\text{rad}} \approx \kappa_{\text{u}}\mathcal{E}_{\text{rad}}'$. So, one can use two general relations

$$\kappa' \approx C^{1/2}, \qquad \epsilon_{\text{rad}}' \approx \frac{\epsilon_{\text{rad}}}{\kappa_{\text{u}}}. \tag{113}$$

Radiative losses of a particle interacting with the radio wave packet are given by Equation (36) with an extra factor of 2 in the stochastic heating regime (B22). Thus, we find

$$\epsilon_{\text{rad}} = \int \dot{\gamma}_e dt = \int \frac{2\sigma_{\text{T}}\tilde{\gamma}^2 U d\xi}{mc(1 + \beta_{\text{D}})} \sim \frac{\sigma_{\text{T}}\tilde{\gamma}^2\mathcal{E}}{4\pi r^2 mc^2}, \tag{114}$$

where we used $dt = d\xi/(1 - \beta_{\text{D}})$ and $\kappa^2(1 - \beta_{\text{D}}) = 1 + \beta_{\text{D}}$. Note that this expression involves the FRB energy $\mathcal{E}$, assuming that the particle interacts with the entire radio packet, i.e. $t_{\text{cross}} \leq r/c$, which corresponds to $C \leq C_{\text{trap}}$.[8]

Using Equations (113) and (114) in Equation (112), we find

$$C_0^{1/2} \sim \frac{\tilde{\gamma}}{\sigma_{\text{u}}}\left(\frac{3}{2} + \psi\right), \qquad \psi \equiv \sqrt{\frac{\sigma_{\text{T}}\mathcal{E}\sigma_{\text{u}}}{4\pi r^2 mc^2\kappa_{\text{u}}}}. \tag{115}$$

Here, $\tilde{\gamma} = \min\{\tilde{\gamma}_{\text{stoch}}, \tilde{\gamma}_{\text{rad}}\}$ depends on $C = C_0$ (section 9.1), and one can find the consistent solution for $\tilde{\gamma}$ and C_0:

$$\tilde{\gamma} = \begin{cases} \tilde{\gamma}_{\text{stoch}} & \psi < 0.7 \\ \tilde{\gamma}_{\text{rad}} & \psi > 0.7 \end{cases} \tag{116}$$

$$C_0 \sim \left[\frac{c\kappa_{\text{u}}}{r_e\omega}\right]^{6/5}\frac{\alpha^{2/5}}{16\sigma_{\text{u}}^4} \times \begin{cases} (3\psi)^{12/5}(3 + 2\psi)^{14/5} & \psi < 0.7 \\ (3 + 2\psi)^4 & \psi > 0.7 \end{cases} \tag{117}$$

with the parameter α given by Equation (86).

The obtained solution holds if it gives $C_0 \gg 1$, and this condition is satisfied at all $r < r_{\text{stoch}}$. Furthermore, C_0 exceeds C_{trap}. Indeed, consider the smallest $C_0^{1/2} \sim 3\tilde{\gamma}_{\text{stoch}}/2\sigma_{\text{u}}$ (Equation 115), which is found in

---

[8] A "deep" trapping regime $t_{\text{cross}} \gg r/c$ is possible if the plasma is trapped in a small leading part of the wave packet, at $\xi_{\text{trap}} \ll T$. In this case, $\mathcal{E}$ in Equation (114) should be replaced by the part of the FRB energy $\mathcal{E}_{\text{trap}}$ contained in the leading part $0 < \xi < \xi_{\text{trap}}$. Self-consistent ξ_{trap} and $\mathcal{E}_{\text{trap}}$ depend on the packet shape.

the non-radiative regime $\psi \ll 0.7$ (small $\mathcal{E}$). Then, using Equation (108) for $\tilde{\gamma}_{\mathrm{stoch}}$, we find

$$C_0 \sim \frac{10^6 \, \mathcal{E}_{39}^{6/5} L_{\mathrm{w},37}^{1/5}}{\nu_9^{8/5} \eta_4^{14/5} R_{\mathrm{LC},10}^{14/5}} \times \begin{cases} 1 & r < R_{\mathrm{sat}} \\ (R_{\mathrm{sat}}/r)^{14/5} & r > R_{\mathrm{sat}} \end{cases}$$

(118)

where $R_{\mathrm{sat}} = \eta^{1/3} R_{\mathrm{LC}} \approx 2 \times 10^{11} \, \eta_4^{1/3} R_{\mathrm{LC},10} \,\mathrm{cm}$ is the radius where the wind Lorentz factor γ_{u} approaches $\eta^{1/3}$ (Equation 83). It is easy to verify that $C_0 > C_{\mathrm{trap}}$ at all $r < r_{\mathrm{stoch}}$. So, FRBs emitted in the wind at $r < r_{\mathrm{stoch}}$ immediately trap the wind plasma.

Two aspects of the trapping regime should be noted: (1) The large value of C_0 is found using the full FRB energy $\mathcal{E} \sim LT$ in the parameter ψ. When $C_0 \gg C_{\mathrm{trap}}$, the plasma becomes trapped in a small leading part of the radio wave packet with $\mathcal{E}_{\mathrm{trap}} \ll \mathcal{E}$ (see footnote 8), avoiding interaction with its main part.
(2) The trapping regime holds unless the FRB becomes strongly damped by its interaction with the wind. Damping allows the plasma to move through the wave packet while consuming its energy, avoiding trapping. The parameter space where FRBs are damped is evaluated below.

10. FRB ENERGY LOSSES

Consider first FRB energy losses $\Delta\mathcal{E}'$ in frame $\mathcal{K}'$ where the upstream plasma is at rest. The corresponding momentum losses are $\Delta\mathcal{E}'/c$.

Let the radio wave packet interact with $\Delta\mathcal{N}$ particles. The momentum lost by the radio wave is the sum of momentum gained by the MHD flow and momentum waisted by the energized plasma particles to radiation,

$$\frac{\Delta\mathcal{E}'}{c} = \Delta\mathcal{N} \, \frac{T_{\mathrm{MHD}}^{t'r'}}{cn'} + \beta_{\mathrm{D}}' \frac{\mathcal{E}_{\mathrm{rad}}'}{c}.$$

(119)

The radiated energy per particle is $\epsilon_{\mathrm{rad}}' mc^2 \equiv \mathcal{E}_{\mathrm{rad}}'/\Delta\mathcal{N}$. This gives

$$\frac{\Delta\mathcal{E}'}{mc^2 \Delta\mathcal{N}} \approx \beta_{\mathrm{D}}' \left[\gamma_{\mathrm{D}}'(1 + w + \sigma_{\mathrm{u}}\kappa') + \epsilon_{\mathrm{rad}}' \right].$$

(120)

Note that $\beta_{\mathrm{D}}' = (\kappa'^2 - 1)/(\kappa'^2 + 1)$ and $\kappa' \approx \tilde{C}$, where $\tilde{C} = \tilde{\rho}/\tilde{\rho}_{\mathrm{u}}$ is the proper compression factor. Thus, Equation (120) yields

$$\frac{\Delta\mathcal{E}'}{mc^2 \Delta\mathcal{N}} \approx (\tilde{C}^2 - 1)\left(\frac{1+w}{2\tilde{C}} + \frac{\sigma_{\mathrm{u}}}{2} + \frac{\epsilon_{\mathrm{rad}}'}{\tilde{C}^2 + 1} \right).$$

(121)

Proper compression $\tilde{C}$ is related to compression C in the lab frame by $C \approx \tilde{C}^2$ (Equation 96). Wave energy in the lab frame is $\mathcal{E} = \kappa_{\mathrm{u}}\mathcal{E}'$, so $\Delta\mathcal{E}' = \Delta\mathcal{E}/\kappa_{\mathrm{u}}$. Radiative losses in the lab frame and frame $\mathcal{K}'$ are also related by $\mathcal{E}_{\mathrm{rad}}/\mathcal{E}_{\mathrm{rad}}' \approx \kappa_{\mathrm{u}}$. Using these relations, one can rewrite Equation (121) in terms of the lab-frame quantities:

$$\frac{\Delta\mathcal{E}}{mc^2 \Delta\mathcal{N} \kappa_{\mathrm{u}}} \approx (C-1)\left[\frac{1+w}{2\sqrt{C}} + \frac{\sigma_{\mathrm{u}}}{2} + \frac{\epsilon_{\mathrm{rad}}}{(C+1)\kappa_{\mathrm{u}}} \right].$$

(122)

As the FRB propagates to a radius r, it interacts with $\Delta\mathcal{N}$ wind particles given by

$$\Delta\mathcal{N} \approx (1 - \beta_{\mathrm{u}})\frac{r}{c}\dot{\mathcal{N}} \approx \frac{2rL_{\mathrm{w}}}{mc^3 \eta \kappa_{\mathrm{u}}^2}.$$

(123)

Equations (122) and (123) determine the FRB energy losses $\Delta\mathcal{E}$ anywhere in the wind, expressed as a function of the compression factor C. Enthalpy $w \approx (3/2)\tilde{\gamma}$ is controlled by the heating regime: $\tilde{\gamma} = (1 + a^2)^{1/2}$ at $r > r_{\mathrm{stoch}}$, and $\tilde{\gamma}$ is given by Equation (108) at $r < r_{\mathrm{stoch}}$.

It is easy to verify that losses are negligible, $\Delta\mathcal{E} \ll \mathcal{E}$, in the zone of regular heating $r > r_{\mathrm{stoch}}$. Thus, FRB damping in the wind may only occur in the zone of stochastic heating, $r < r_{\mathrm{stoch}}$.

Using $w \approx (3/2)\tilde{\gamma} \gg 1$ and $C \gg 1$, we find from Equation (122):

$$\Delta\mathcal{E} \approx \frac{rL_{\mathrm{w}}}{2c\,\eta\gamma_{\mathrm{u}}} \left[\frac{3}{2}\tilde{\gamma}\sqrt{C} + \sigma_{\mathrm{u}}C + \frac{\sigma_{\mathrm{T}}\tilde{\gamma}^2 \mathcal{E}}{4\pi r^2 mc^2 \gamma_{\mathrm{u}}} \right].$$

(124)

For an FRB with luminosity L and energy $\mathcal{E} \sim LT$, we find $\tilde{\gamma}(r, C)$ from Equation (108) at radii $r < r_{\mathrm{stoch}}$, and then find $\Delta\mathcal{E}(r, C)$ from Equation (124).

The FRB is strongly damped if $\Delta\mathcal{E}$ approaches $\mathcal{E}$. Damping begins in the leading part of the FRB $\xi \ll T$, as the plasma entering the radio wave packet consumes its local energy $\mathcal{E}(\xi) \sim 4\pi r^2 U(\xi) c \xi$ and makes the deep trapping regime $C \gg C_{\mathrm{trap}}$ unsustainable. Damping succeeds in killing the FRB when it enables the plasma to keep going in ξ and crossing the entire wave packet, which corresponds to $\Delta\mathcal{E} \sim \mathcal{E}$ and marginal trapping, $C \approx C_{\mathrm{trap}}$. Therefore, the condition for marginal damping is

$$\frac{\Delta\mathcal{E}(r, C_{\mathrm{trap}})}{\mathcal{E}} \approx 1.$$

(125)

It defines the boundary of the parameter space where FRBs are strongly damped. One can show that $\Delta\mathcal{E}(r, C_{\mathrm{trap}})/\mathcal{E}$ is a decreasing function of $\mathcal{E}$, so strong damping occurs for FRBs with energies $\mathcal{E}$ below a critical value $\mathcal{E}_{\mathrm{esc}}(r)$ defined by Equation (125) and the corresponding critical luminosity is $L_{\mathrm{esc}} \sim \mathcal{E}_{\mathrm{esc}}/T$. The damping region on the r-L plane is shown in Figure 8.

It is useful to examine more closely the loss $\Delta\mathcal{E}$ stated in Equation (124). The three terms in the square brackets correspond to three contributions,

$$\Delta\mathcal{E} = \mathcal{E}_{\mathrm{p}} + \mathcal{E}_{\mathrm{mag}} + \mathcal{E}_{\mathrm{rad}},$$

(126)

where $\mathcal{E}_{\mathrm{p}} \propto \tilde{\gamma}$ is the energy kept by the plasma particles, $\mathcal{E}_{\mathrm{mag}} \propto \sigma_{\mathrm{u}}$ is the energy used to compress the wind magnetic field, and $\mathcal{E}_{\mathrm{rad}} \propto \tilde{\gamma}^2$ is the radiative losses. Let us compare radiative losses $\mathcal{E}_{\mathrm{rad}}$ with $\mathcal{E}_{\mathrm{p}}$ and $\mathcal{E}_{\mathrm{mag}}$.

It is easy to see that $\mathcal{E}_{\mathrm{rad}} > \mathcal{E}_{\mathrm{p}}$ if $\tilde{\gamma}_{\mathrm{rad}} < \tilde{\gamma}_{\mathrm{stoch}}$; in this regime, the plasma radiates more energy than it keeps. This occurs at radii that satisfy the condition given in Equation (109). With $C = C_{\mathrm{trap}}$, it can be stated as

$$\mathcal{E}_{\mathrm{rad}} > \mathcal{E}_{\mathrm{p}}: \quad r < 2 \times 10^{11} \frac{\mathcal{E}_{39}^{20/47} T_{\mathrm{ms}}^{5/47} L_{\mathrm{w},37}^{1/47}}{\gamma_{\mathrm{u}}^{4/47} \nu_9^{8/47}} \,\mathrm{cm}.$$
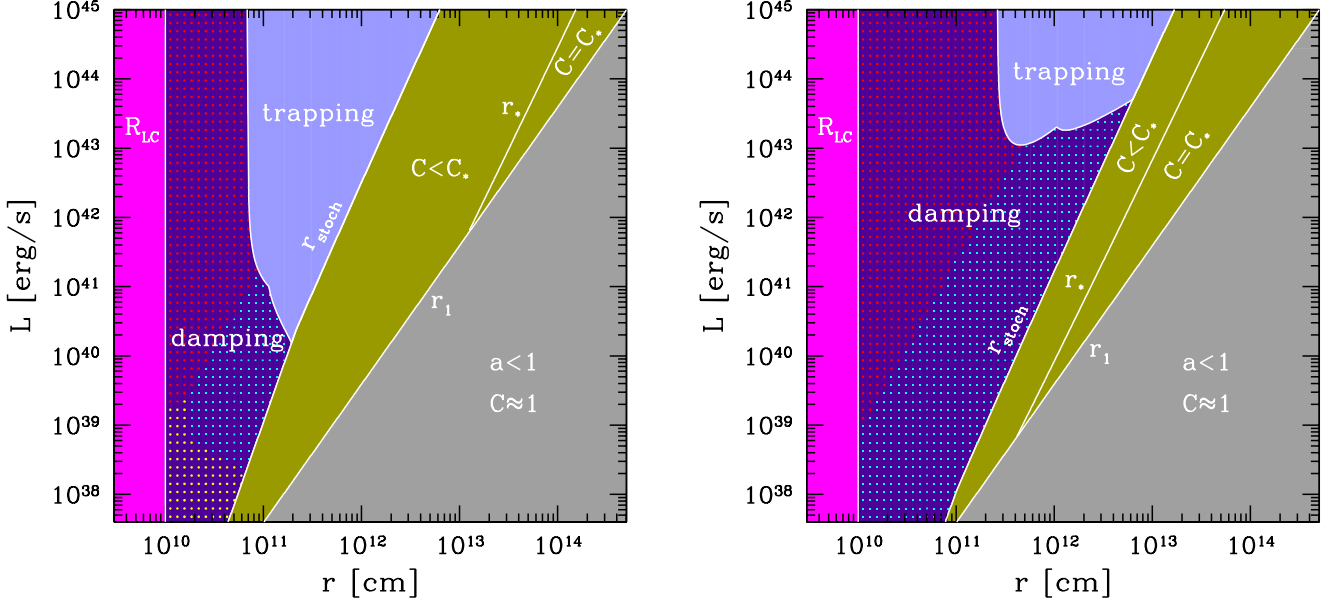
(127)

Figure 8. Regimes of FRB propagation through the wind ($r > R_{\rm LC}$), shown on the r-L plane, for FRBs with emission frequency $\nu = 1\,{\rm GHz}$ and duration $T = 1\,{\rm ms}$. The two plots assume the wind energy parameter $\eta = 10^4$ (left) and $\eta = 10^3$ (right). The magenta region $r < R_{\rm LC}$ indicates the closed magnetosphere. FRBs emitted inside the magnetosphere experience strong radiative damping (Beloborodov 2024). FRBs emitted at radii $R_{\rm LC} < r < r_{\rm stoch}$ induce fast stochastic heating and compression of the wind. In the light purple region, FRBs trap the wind plasma, carrying it in a leading part of the wave packet and avoiding significant energy losses. In the deep purple region, FRBs are damped: their energy is consumed by heating and compressing the wind plasma, with radiative losses. The colored dots indicate the dominant damping channel: radiative losses $\mathcal{E}_{\rm rad}$ (red dots), energy kept by the plasma $\mathcal{E}_{\rm p}$ (cyan dots) and energy spent to compress the wind magnetic field $\mathcal{E}_{\rm mag}$ (yellow dots). In the olive zone, $r_{\rm stoch} < r < r_1$, the wind is still heated to a relativistic enthalpy $w \gg 1$; however, here heating occurs in the regular regime (particles oscillate in the radio wave instead of stochastically gaining energy) with the moderate $w \approx (3/2)a$ and a weaker compression. At radii $r_\star < r < r_1$, the compression factor is $C = C_\star \approx 1 + a_0^2$. The FRB strength parameter $a = a_0/\sqrt{2}$ drops below unity outside r_1 (grey region).

The ratio $\mathcal{E}_{\rm rad}/\mathcal{E}_{\rm mag}$ equals the ratio of the third and second terms in the brackets in Equation (124). Using $C = C_{\rm trap}$ and $\tilde{\gamma} = \tilde{\gamma}_{\rm rad}$ (i.e. assuming $\mathcal{E}_{\rm rad} > \mathcal{E}_{\rm p}$), we find

$$\mathcal{E}_{\rm rad} > \mathcal{E}_{\rm mag}: \quad r < 10^{11} \gamma_{\rm u}^{16/27} \frac{\mathcal{E}_{39}^{10/27} T_{\rm ms}^{5/27} L_{\rm w,37}^{1/27}}{\eta_4^{10/27} \nu_9^{8/27}} \; {\rm cm}. \tag{128}$$

$\mathcal{E}_{\rm rad}$ dominates the FRB losses at radii that satisfy both conditions stated in Equations (127) and (128).

11. SUMMARY

The basic physics problem studied in this paper is how a strong ($a_0 \gg 1$) electromagnetic wave packet accelerates an MHD fluid. For weak electromagnetic waves ($a_0 \ll 1$), the acceleration effect is well known as the radiation pressure force, used in astrophysics e.g. to define the Eddington limit. For strong waves, the acceleration effect was previously calculated in unmagnetized plasmas; the $e^\pm$ plasma then becomes compressed in the wave packet by the factor $C \approx 1 + a_0^2$. A similar problem for a magnetized plasma was poorly understood. The present paper developed a method to solve this problem, obtained sample numerical solutions, and provided a physical picture of the wave-plasma interaction. Two key facts help solve the problem: (1) the wave strength parameter a_0 controls the plasma enthalpy as shown in section 3, and (2) quantity $\mathcal{Q}_- = \mathcal{E} - c\mathcal{P}$ (where $\mathcal{E}$ is energy and $\mathcal{P}$ is momentum) is conserved in the wave-plasma interaction because the wave has $\mathcal{Q}_- = 0$ and cannot transfer $\Delta\mathcal{Q}_- \neq 0$ to the MHD fluid.

A first estimate would suggest that plasma with a sufficiently large magnetization σ is not strongly compressed by the electromagnetic wave, since the deposited momentum is proportional to the small plasma density while compression requires work to be done against the large background magnetic pressure (Beloborodov 2021; see also section 6.1). The actual solution demonstrates that this expectation holds initially, when the wave packet begins to interact with the plasma. Later, the propagating wave gradually develops a large compression factor C due to a curious "memory" effect described in section 6. Given a sufficient time $t_\star \propto C\sigma$ the compression front relaxes to a steady state with

$C = C_\star \approx 1 + a_0^2$ independent of σ. However, large $C_\star$ (implied by large a_0) is not reached if $t_\star$ exceeds the wave propagation time.

Besides the peculiar gradual evolution of the propagating wave packet, the background magnetic field brings another special feature that dramatically changes the wave-plasma interaction: compression increases the gyro-frequency and triggers strong stochastic heating of the plasma by the electromagnetic wave. The heating boosts momentum deposition, enhancing acceleration and compression of the MHD fluid in the wave packet.

We have used the obtained results to examine FRB interaction with a magnetized wind flowing from the central object (a neutron star). Our conclusions are summarized below and illustrated in Figure 8.

FRBs propagating at radii $R_{\rm LC} < r < r_{\rm stoch}$ have a huge effect on the wind medium. They heat the wind up to an average Lorentz factor $\tilde{\gamma} \sim 10^3 a_0$ (measured in the fluid rest frame), and accelerate it to a bulk Lorentz factor exceeding $\gamma_{\rm trap} \sim (r/cT)^{1/2}$, which implies trapping of the wind plasma inside the radio wave packet. The energy per particle in the heated plasma $\gamma_{\rm trap}\tilde{\gamma}mc^2$ (measured in the static lab frame) is in the TeV range. Thus, the FRB-wind interaction converts the radio-wave energy into high energy particles, which experience radiative losses. A fraction of FRB energy is also spent to compress the wind magnetic field. Only sufficiently bright FRBs survive the energy losses (Figure 8).

The FRB-wind interaction changes at larger radii: at $r = r_{\rm stoch}$ (Equation 102) there is a sharp transition from stochastic heating to regular heating (particle oscillation in the wave), which sustains a moderate $\tilde{\gamma} \sim a_0$. Energy losses of the radio wave are negligible at $r > r_{\rm stoch}$. FRBs emitted in this zone still induce strong bulk acceleration of the wind plasma. Here, instead of trapping the plasma, the FRB drives an MHD compression wave in the wind. At $r > r_\star$ (Equation 93), the compression wave is quasisteady ($r/c \gg t_\star$), and the compression factor equals $C_\star \approx 1 + a_0^2$.

The picture of FRB-wind interaction described here partially agrees with the results of Sobacchi et al. (2024), but only at large radii $r > r_\star \sim 10^{13} L_{42}^{1/3}$ cm. Sobacchi et al. (2024) assumed a quasisteady compression front with regular plasma oscillations in the radio wave, and obtained the compression factor $C_\star \approx a_0^2 \propto r^{-2} \gg 1$. Their solution agrees with our result $C_\star \approx 1 + a_0^2$ found at $r > r_\star$. Sobacchi et al. (2024) incorrectly applied this solution at smaller r where compression $C_\star$ becomes huge and can require energy deposition exceeding the FRB energy, which led them to conclude that FRBs emitted at $r \lesssim 10^{12}$ cm are damped.[9] In fact, the steady-front solution $C = C_\star$ becomes irrelevant at

$r < r_\star \sim 10^{13}$ cm because the relaxation time $t_\star$ exceeds the propagation time r/c. Furthermore, the compression front at $r < r_{\rm stoch}$ is changed by stochastic heating, trapping, and radiative losses (section 9).

The results summarized in Figure 8 imply interesting constraints on FRB emission models. In particular, they exclude scenarios that place the radio source at radii $r < r_{\rm damp} \sim 10^{11}$ cm and rely on free FRB propagation through the magnetar wind. Thus, the previously found damping zone $r < R_{\rm LC}$ (Beloborodov 2021, 2024; Golbraikh & Lyubarsky 2023) is extended to $r_{\rm damp} \sim 10^{11}$ cm. The exact value of $r_{\rm damp}$ varies around 10^{11} cm for the relevant values of wind parameter $\eta = L_{\rm w}/\dot{\mathcal{N}}mc^2$ around 10^4. We find that $r_{\rm damp}$ slowly decreases with increasing $\eta > 10^4$. The compression and damping effects are particularly strong in winds with $\eta < 10^4$.

The obtained constraints support the explosion scenario for FRB emission. In all cases, the central engine must be the inner magnetosphere ($r \lesssim 10^8$ cm), which possesses sufficient energy to power the observed burst. The energy liberated in the inner magnetosphere must be relocated outside $r_{\rm damp}$ before the FRB is released into the surrounding medium. This is accomplished by the sudden ejection of a powerful macroscopic electromagnetic pulse, which expands to large radii. The ejected pulse is capable of producing FRB emission by two known mechanisms. (1) The pulse propagation through a preexisting current sheet near $R_{\rm LC}$ results in small-scale perturbations imprinted in the ejecta. These perturbations may be released as GHz radio waves when the ejecta expands to a large radius (Lyubarsky 2020). (2) FRB is emitted by synchrotron maser in a shock created by the expanding electromagnetic pulse (Beloborodov 2017, 2020). Such FRBs do not experience significant damping, because GHz emission occurs at $r \sim 10^{13} - 10^{14}$ cm, well outside $r_{\rm damp}$. The shock was also proposed to produce radio waves via mode conversion when it propagates in a medium with small-scale fluctuations (Thompson 2023).

In addition to plasma acceleration and compression studied in this paper, the ambient medium may be strongly affected by the nonlinear development of self-modulation instabilities of the radio wave (Sobacchi et al. 2023), investigated so far for waves with $a_0 < 1$. Instabilities in the wind zone with $a_0 > 1$ are poorly understood and will require future work.

---

[9] Note though that energy consumption implied by $C_\star \approx 1 + a_0^2$ is reversible, since $C_\star$ comes back to unity behind the wave packet. Damping is usually inefficient for reversible processes.

REFERENCES

Beloborodov, A. M. 2017, ApJL, 843, L26, doi: 10.3847/2041-8213/aa78f3

—. 2020, ApJ, 896, 142, doi: 10.3847/1538-4357/ab83eb

—. 2021, ApJL, 922, L7, doi: 10.3847/2041-8213/ac2fa0

—. 2022, PhRvL, 128, 255003, doi: 10.1103/PhysRevLett.128.255003

—. 2024, ApJ, 975, 223, doi: 10.3847/1538-4357/ad698c

Bulanov, S. V., Esirkepov, T. Z., Kando, M., et al. 2015, Plasma Physics Reports, 41, 1, doi: 10.1134/S1063780X15010018

Cerutti, B., & Beloborodov, A. M. 2017, SSRv, 207, 111, doi: 10.1007/s11214-016-0315-7

Golbraikh, E., & Lyubarsky, Y. 2023, ApJ, 957, 102, doi: 10.3847/1538-4357/acfa78

Gunn, J. E., & Ostriker, J. P. 1971, ApJ, 165, 523, doi: 10.1086/150919

Huang, Y.-C., Zhong, S.-Q., & Dai, Z.-G. 2024, ApJ, 966, 97, doi: 10.3847/1538-4357/ad39e7

Landau, L. D., & Lifshitz, E. M. 1975, The classical theory of fields

Lyubarsky, Y. 2020, ApJ, 897, 1, doi: 10.3847/1538-4357/ab97b5

Lyubarsky, Y., & Kirk, J. G. 2001, ApJ, 547, 437, doi: 10.1086/318354

Petroff, E., Hessels, J. W. T., & Lorimer, D. R. 2019, A&A Rv, 27, 4, doi: 10.1007/s00159-019-0116-6

Sobacchi, E., Iwamoto, M., Sironi, L., & Piran, T. 2024, A&A, 690, A332, doi: 10.1051/0004-6361/202451725

Sobacchi, E., Lyubarsky, Y., Beloborodov, A. M., Sironi, L., & Iwamoto, M. 2023, ApJL, 943, L21, doi: 10.3847/2041-8213/acb260

Thompson, C. 2023, MNRAS, 519, 497, doi: 10.1093/mnras/stac3565